

ORIGINAL ARTICLE

Open Access



A hypothesis of the obliquely subducted Gagua Ridge below Nanao Basin based on uplifted structures in Ryukyu forearc

Jia-Ming Deng¹, Tan Kin Wang^{2*}, Sebastian Wege², Wan Ting Hu² and Yi Jie Deng²

Abstract

At the southernmost part of the Ryukyu subduction zone, six long-offset multi-channel seismic profiles were collected across three forearc basins and the southern Ryukyu accretionary prism during the TAIGER experiment in 2009 and the TAICRUST project in 1995. These profiles were reprocessed to generate pre-stack depth migration (PSDM) sections. In addition, two velocity-interface models were obtained by reanalyzing active source data recorded from 28 ocean-bottom seismometers during the same TAIGER experiment, in consideration of the PSDM sections and previous tomography models. Due to the northwest convergence of the Philippine Sea Plate (PSP), it is suggested that the Gagua Ridge may have been obliquely subducting northwestward beneath the Ryukyu prism and below the Nanao Basin. The PSDM sections and the velocity-interface models indicate the subducted Gagua Ridge causing the uplift of the sedimentary basement and the lower crustal structure below the Nanao Basin. The sedimentary and crustal structures near $\sim 122.5^\circ$ E beneath the Nanao Basin were also uplifted where shallow earthquakes had occurred by the oblique subduction of the Gagua Ridge depicted in the isopach map of the crust. Furthermore, a recent earthquake ($M_w \sim 6.0$) occurred near the northeast coast of Taiwan in 2018 at a depth of approximately 12 km below the Hsincheng Ridge. Our study suggests that this earthquake was caused by a thrust fault near the décollement, which might have been formed by the subduction of the PSP.

Keywords Forearc basin, Gagua Ridge, Long-offset multi-channel seismic, Ocean-bottom seismometers, Ryukyu Trench

1 Introduction

In the southernmost Ryukyu subduction zone, the 25-km-wide Gagua Ridge with a height of ~ 4 km above the seafloor, is subducted beneath the southernmost Ryukyu Trench, the Ryukyu accretionary prism and the forearc basins causing earthquakes in the overlying plate (Konstantinou et al. 2011; Theunissen et al. 2012).

The southernmost Ryukyu subduction system has been transformed from subduction to collision due to westward collision and northward subduction of the Philippine Sea Plate (PSP) (Lallemand and Tsien 1997). In the westernmost part of the Nankai Trough, the 70-km-wide Kyushu-Palau Ridge with a height of ~ 1 km above the seafloor has been subducted below the Nankai Trough to induce thrust-type earthquakes with a magnitude of 6 or 7 at the contact zone between the subducted Kyushu-Palau Ridge and the base of the overriding plate (Park et al. 2009). This is similar to the Ninety East Ridge in the Andaman subduction zone (Subrahmanyam et al. 2008) and the Juan Fernández Ridge in the Chilean subduction zone (von Huene and Ranero 2003), both of which are subducted beneath an accretionary forearc causing

*Correspondence:

Tan Kin Wang
tkwang@mail.ntou.edu.tw

¹ Taiwan Ocean Research Institute, National Applied Research Laboratories, No. 500, Zhongda Road, Kaohsiung, Taiwan R.O.C.

² Institute of Earth Sciences, National Taiwan Ocean University, No. 2, Pei-Ning Road, Keelung, Taiwan R.O.C.



earthquakes. Furthermore, Zeumann and Hampel (2015, 2016) provided a systematic discussion on the forearc deformation, caused by the subduction of those aseismic ridges with the accretive forearcs, depending on the direction of plate convergence, angle of subduction, and shape of the oceanic ridges. Moreover, subducted ridges may play various roles, not only as asperities (Cloos 1992) but also as a barrier (Kodaira et al. 2000), a creep zone (Mochizuki et al. 2008), and even an inducer of intra-slab faulting (Arai et al. 2017). Thus, the southern end of the Ryukyu subduction system with the Gagua Ridge is an interesting region for studying plate dynamics and seismogenic structures in a ridge-subducted forearc setting.

During 1998–2021, three major earthquakes with $M_w \geq 6.0$ (the red-framed squares in Fig. 1a) were located

below the Hsincheng Ridge and the forearc basins in the southernmost Ryukyu subduction zone. In 2001, one of these earthquakes ($M_w \sim 6.8$) occurred at a shallow depth of ~ 25 km below the Nanao Basin due to a normal faulting mechanism with some strike-slip components rupturing at the flank of the subducted Gagua Ridge (Konstantinou et al. 2011). The two other earthquakes ($M_w \sim 6.2$ and ~ 6.0) occurred at depths of ~ 25 km below the Nanao Basin in 2004 and ~ 12 km below the Hsincheng Ridge in 2018, respectively, along thrust faults due to subduction of the PSP. Furthermore, many shallow earthquakes at depths of 0–30 km (Font et al. 2004; BATS, Institute of Earth Sciences, Academia Sinica, Taiwan, 1996) have occurred below the forearc basins in the southernmost Ryukyu subduction zone (Fig. 1). We

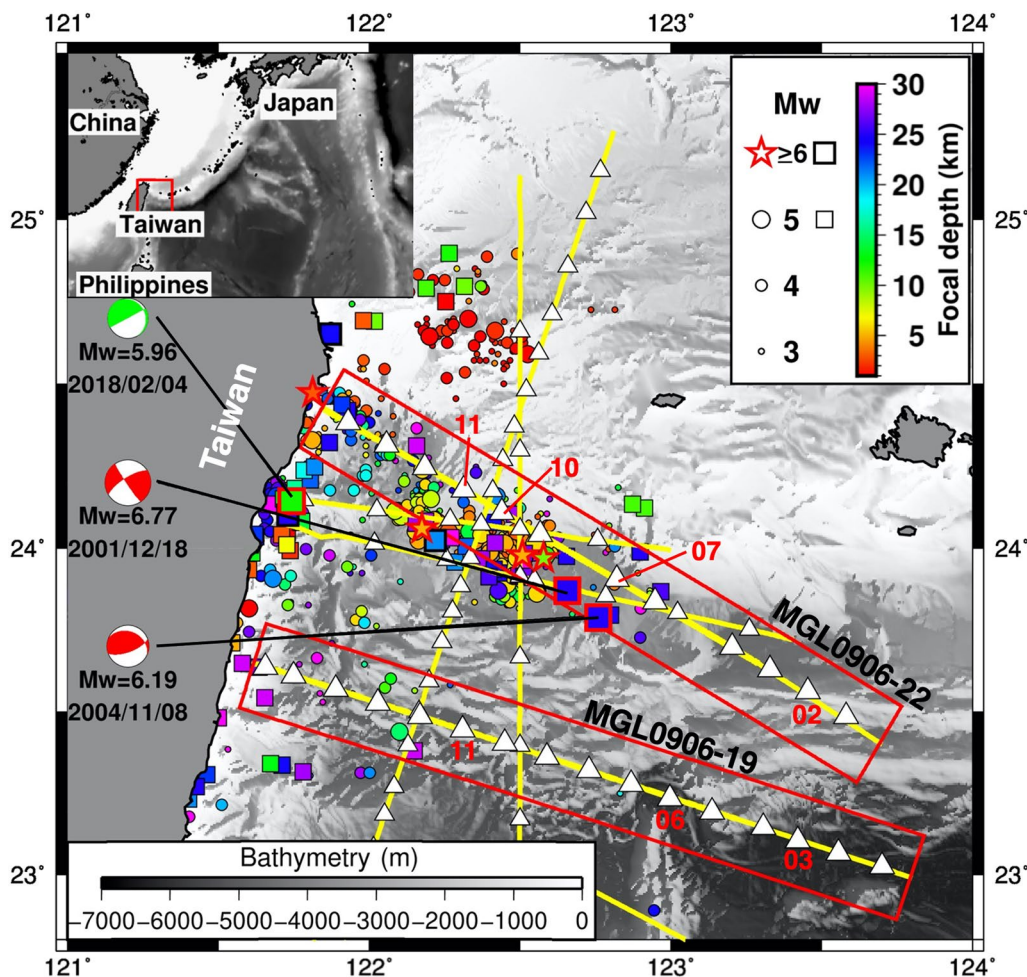


Fig. 1 The earthquakes in 1992–1997 (relocated by Font et al. 2004) and 1998–2021 ($M_w \geq 5$ from BATS, Institute of Earth Sciences, Academia Sinica, Taiwan, 1996) respectively indicated by the circles and squares on the bathymetry map at the southernmost Ryukyu subduction zone. The $M_w \geq 6$ earthquakes from Font et al. 2004 are marked by the stars. The earthquakes along MGL0906-19 and MGL0906-22 in the red rectangles with widths of 30 km are projected on the P-wave velocity-interfaces models (Figs. 9 and 10). The red numbers show where the images of OBS data in Figs. 7, 8, Additional file 1: Figs. S7 and S8 are located

reanalyzed and integrated the long-offset multi-channel seismic (LMCS) and ocean-bottom seismometer (OBS) data with active sources to image the complex structures beneath the forearc basins in this subduction zone, and to understand how these major earthquakes were induced at shallow depths and why they usually occurred below the forearc basins to form earthquake clusters (Theunissen et al. 2012).

Several tomographic models of the deep crust (> 30 km) have been built based on earthquake data (Chin et al. 2016; Gautier et al. 2019; Huang et al. 2014; Kuo-Chen et al. 2012; Wu et al. 2009). However, because of limited ray coverage, the models of the shallow (0–30 km) structures in the southernmost Ryukyu subduction zone, such as the accretionary prism and other subducted structures, showed low-resolution images. Moreover, the crustal structures beneath the Nanao Basin and Nanao Basement Rise show less evidence of subduction of the PSP. For the previous OBS models along MGL0906-19 (van Avendonk et al. 2014) and MGL0906-22 (van

Avendonk et al. 2016), the sedimentary structures were less constrained because the pre-stack depth migration (PSDM) sections from the LMCS data processing were not considered. Furthermore, van Avendonk et al. (2014, 2016) used only the first arrivals and the arrivals reflected at the Moho from the OBS data with travel-time errors of 135–145 ms. They did not constrain the intra-crustal interfaces in the tomographic models and emphasized the interpretation of crustal structures near Taiwan Island. Thus, the sedimentary structures were imaged with PSDM sections, and the velocity-interface models were reanalyzed by considering the PSDM section and tomography models (van Avendonk et al. 2014, 2016) in the southernmost Ryukyu subduction zone. Furthermore, six OBS profiles collected during the TAICRUST project of 1995 and TAIwan Integrated GEodynamics Research (TAIGER) in 2009 (Fig. 2) were integrated to observe variations in sedimentary and crustal thickness and delineate the geometry of the Ryukyu accretionary prism, crustal deformation below the forearc basins, and

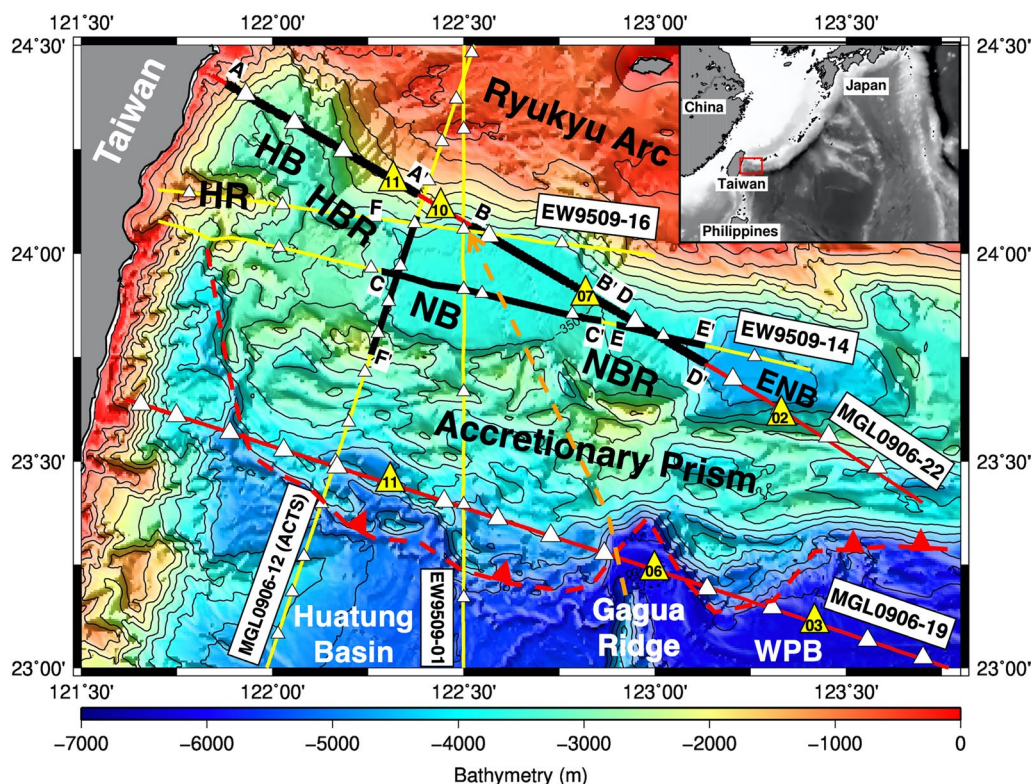


Fig. 2 The bathymetry map with seismic lines at the southernmost Ryukyu Trench. During 1995 TAICRUST and 2009 TAIGER projects, LMCS data were collected, processed, and integrated along EW9509-01, EW9509-14, EW9509-16, MGL0906-12, MGL0906-19, and MGL0906-22. OBSs are indicated by the white triangles. The capital letters of A, B, C, D, E, F and A', B', C', D', E', F' indicate respectively the starting point and endpoint of the MCS data shown in Figs. 3, 4, 5, 6, Additional file 1: Figs. S5 and S6. The yellow triangles show where the images of OBS data in Figs. 7, 8, Additional file 1: Figs. S7 and S8 are located. The red dashed line indicates the Ryukyu Trench with the red triangles which show the direction of subduction. The Gagua Ridge might be obliquely subducted toward the NW direction indicated by the orange dashed-line arrow. The contour lines are bathymetry with the contour interval of 500 m. WPB: West Philippine Basin, HR: Hsincheng Ridge, HB: Hoping Basin, HBR: Hoping Basement Rise, NB: Nanao Basin, NBR: Nanao Basement Rise, ENB: East Nanao Basin

the shape of the Ryukyu Arc. These results will be further discussed to clarify the crustal structures below the Hopping Basement Rise and Nanao Basin associated with a detached block of the Luzon Arc, subduction of an oceanic relief (either an exotic block, seamount, or oceanic crust sliver) (Font and Lallemand 2009), buckling of the subducted slab (Wang et al. 2004) or an off-scraped part of the Luzon Arc (Font et al. 2001; Lallemand et al. 2013). Moreover, the Gagua Ridge possibly subducted northwardly (Zeumann and Hampel 2016), or northwardly to form the Nanao Basement Rise (Font et al. 2001). In this paper, a hypothesis is proposed to explain why the shallow earthquakes usually occurred below the forearc basins based on the complex structures of the velocity-interface models imaged from LMCS and OBS data.

2 Tectonic setting

The westernmost PSP, consisting of the Luzon Arc, Hualung Basin, Gagua Ridge, and West Philippine Basin, is northwardly subducting beneath the Eurasian Plate (Chou et al. 2009; Wu et al. 2009; Lallemand 2014) owing to the northwestward convergence of the PSP (Taylor and Goodliffe 2004; Deschamps and Lallemand 2002). The Ryukyu Trench, Ryukyu accretionary prism, forearc basins, and Ryukyu Arc have been formed as parts of the Ryukyu subduction system due to the subduction of the westernmost PSP (Bowin et al. 1978; Lundberg et al. 1997). The Ryukyu Arc extends southward beneath the Ryukyu accretionary prism based on the velocity-interface model across the southernmost Ryukyu system (e.g., Wang et al. 2004; Klingelhoefer et al. 2012). Because plate coupling is much stronger in the southernmost Ryukyu subduction zone, the overriding plate may have been bent and dragged deeper along the plate interface to generate earthquakes by the splay-fault systems in the tsunami-genic zone (Hsu et al. 2013). Similarly, splay-fault systems associated with large earthquakes have been found in the subduction zones of Sunda (Sibuet et al. 2007), Nankai

(Park et al. 2002; Moore et al. 2007), Ecuador-Colombia (Collot et al. 2004), and Alaska (Plafker 1972).

In this forearc region, Font and Lallemand (2009) observed several normal faults indicating that the Hopping Basement Rise is still active. Because the PSP is subducted beneath the Ryukyu Arc, many earthquakes have occurred at depths of 12–22 km beneath the eastern Hopping Basement Rise, the Nanao Basin, and the slope of the Ryukyu Arc along the subduction interface (Font and Lallemand 2009). Furthermore, most of these earthquakes show pure and oblique thrust-type focal mechanisms prevailing around the forearc basins owing to trench-perpendicular compression (Konstantinou et al. 2011). Associated with this plate subduction, several earthquakes have occurred on thrust faults at depths of between 10 and 35 km below the Nanao Basin, where the seismogenic structure has been imaged as a northwardly subducted plate with a dip angle of ~25 degrees, based on velocity-interface models (Wang et al. 2001, 2004). The southward-dipping antithetic thrusts were imaged with an average dip of 15 degrees at depths of 15–25 km in the basement of the overriding plate based on the focal mechanisms along the Ryukyu arc (Kao and Chen 1991).

3 Data and method

LMCS and OBS data with active sources were analyzed to image the sedimentary and crustal structures at depths of 0–30 km. During the 1995 TAICRUST and 2009 TAIGER projects, LMCS data along EW9509-01, EW9509-14, EW9509-16, MGL0906-12, MGL0906-19, and MGL0906-22 (Fig. 1) were collected by a 4 km streamer and a 6 km streamer, which received signals from an air-gun array with total volumes of 8425 and 6600 cubic inches, respectively (the details are shown in Table 1). These LMCS data were processed to obtain PSDM sections for the Ryukyu accretionary prism and the forearc basins in the southernmost Ryukyu subduction zone. The velocity models with well-constrained interfaces along EW9509-01 (Wang et al. 2001), EW9509-14 (Wang et al.

Table 1 Parameters of LMCS data

	EW9509-01	EW9509-14	EW9509-16	MGL0906-12	MGL0906-22
Research Vessel	Maurice Ewing	Maurice Ewing	Maurice Ewing	Marcus G. Langseth	Marcus G. Langseth
Project	1995 TAICRUST	1995 TAICRUST	1995 TAICRUST	2009 TAIGER	2009 TAIGER
Streamer Length (channel)	3975 m (160)	3875 m (156)	3875 m (156)	6000 m (468)	6000 m (468)
Receiver spacing	25 m	25 m	25 m	12.5 m	12.5 m
Recording length	16 s	16 s	16 s	15 s	15 s
Total volume of air-gun array	8425 in ³	8425 in ³	8425 in ³	6600 in ³	6600 in ³
Band-pass filter (Hz)	4-8-70-90	4-8-70-90	4-8-70-90	4-8-64-120	10-22-64-78

2004), EW9509-16 (Wang et al. 2004) and MGL0906-12 (Klingelhoefer et al. 2012) were used to construct the isopach maps of the sedimentary and crustal thickness in this study. OBS data, collected by using an air-gun array with a shooting interval of 60 s along MGL0906-19 and MGL0906-22 (Fig. 2), were reprocessed by considering the PSDM sections to constrain the shallow structures of the velocity-interface models. Intra-crustal interfaces and the Moho along MGL0906-19 and MGL0906-22 were also imaged from travel-time inversion of OBS data (Zelt and Smith 1992) across the Ryukyu accretionary prism and the forearc basins, respectively. Furthermore, these velocity-interface models along MGL0906-19 and MGL0906-22 were integrated into isopach maps for the sediment and crust.

3.1 LMCS data processing

LMCS data were reprocessed through geometry, band-pass filtering (Table 1), and vertical velocity analysis to obtain pre-stack time migration (PSTM) sections (Yilmaz 2001). The ranges of the frequency, used on the band-pass filtering (Table 1), were determined by using the spectral analysis (Tu 2015; Hu 2017). Subsequently, horizons were identified along strong reflectors in the PSTM sections so that we can select P-wave velocities from semblances of the horizontal velocity analysis layer by layer. Residual analysis of the root-mean-square (RMS) velocity was then applied to enhance its reliability (Additional file 1: Fig. S1). For example, the 10 horizons were picked along the strong reflectors in the PSTM section along MGL0906-22 (Additional file 1: Fig. S2) to build the horizontal velocity model. Based on the semblances of the horizontal velocity analysis along MGL0906-22 (Additional file 1: Fig. S3), the picking of P-wave velocities was more difficult in the deeper and more complex structures (white frames in Additional file 1: Fig. S3). Thus, the P-wave velocities were iterated by considering the residual analysis of the RMS velocity (Additional file 1: Fig. S4) and seismic images to obtain a reliable horizontal velocity model. Low concentrations of the semblances for the residual velocity analysis in the deeper and complex structures were observed because of weak signals or near the end of the model (the white frames in Additional file 1: Fig. S4). Moreover, the horizontal velocity was kept simple (Additional file 1: Fig. S3) to get better images of the PSDM section (Fig. 3) without the residual analysis of the RMS velocity because the strata 3 of the old Suao Basin (grey line in Additional file 1: Fig. S2) is the last layer to accumulate the large error from the shallow layers. Based on the flowchart of the LMCS data processing for the PSDM section (Additional file 1: Fig. S1), velocity (1.5–4.2 km/s) models and PSDM sections (Figs. 3, 4, 5, 6, Additional file 1: Figs. S5, and S6)

were obtained through several iterations. However, the low concentrations of semblances for the residual velocity analysis in the deeper and complex structures were still observed because of weak signals or near the two ends of the models (Tu 2015; Hu 2017). In this study, the PSDM sections along MGL0906-22 (Figs. 3, 5 and Additional file 1: Fig. S5), EW9509-14 (Figs. 4 and Additional file 1: Fig. S6), and MGL0906-12 (Fig. 6) were processed and interpreted at areas for which interpretations based on other profiles have not yet been presented (Font et al. 2001; Klingelhoefer et al. 2012; Lallemand et al. 2013).

3.2 OBS data processing

The OBS data along MGL0906-19 (Fig. 7) and MGL0906-22 (Fig. 8) were reprocessed through format transformation, time correction, relocation, spiking deconvolution, gain, and bandpass filtering (1–5–15–20 Hz) to decrease the noise and improve the quality of the signals. Because sea currents usually cause the OBSs to drift away from the dropped location, travel times of the air-gun direct waves were selected from the OBS data to relocate the OBSs on the seafloor along the profiles. Initial models for sedimentary and crustal structures along MGL0906-19 (Fig. 9) and MGL0906-22 (Fig. 10) were built from the PSDM sections (Tu 2015; Hu 2017) and previous OBS models (Wang et al. 2001, 2004; van Avendonk et al. 2014, 2016) near the respective OBS lines. For building the sedimentary interfaces, 4 major unconformities were selected to be interfaces of initial models based on the PSDM sections because the velocity-interface models should be kept simple for travel-time inversion. For example, the sedimentary layers of the initial model in the Hopping Basin along MGL0906-22, the 4 major unconformities (black, white dashed, white, and yellow dashed lines in Figs. 3 and 10) were only selected from the 10 horizons of the PSDM sections (Additional file 1: Fig. S2). Subsequently, the sedimentary interfaces were adjusted by forward modeling, and the calculated arrivals, propagating through sediments, were fitted to the OBS data along MGL0906-19 (Additional file 1: Fig. S7) and MGL0906-22 (Additional file 1: Fig. S8). To update the crustal structures of the initial model, we selected the reflected and refracted arrivals through the upper, middle, and lower crust, and the upper mantle (Figs. 7 and 8) and inverted the model layer-by-layer (Zelt and Smith 1992) to reduce the travel-time errors (Tables 2 and 3). Finally, the densities of the reflected and refracted rays (Additional file 1: Figs. S9a and S10a) were used to justify the robustness of the interfaces and velocities in the OBS model and to reveal the P-wave velocity-interface model where the velocities are fully, less, or poorly constrained (Deng et al. 2012).

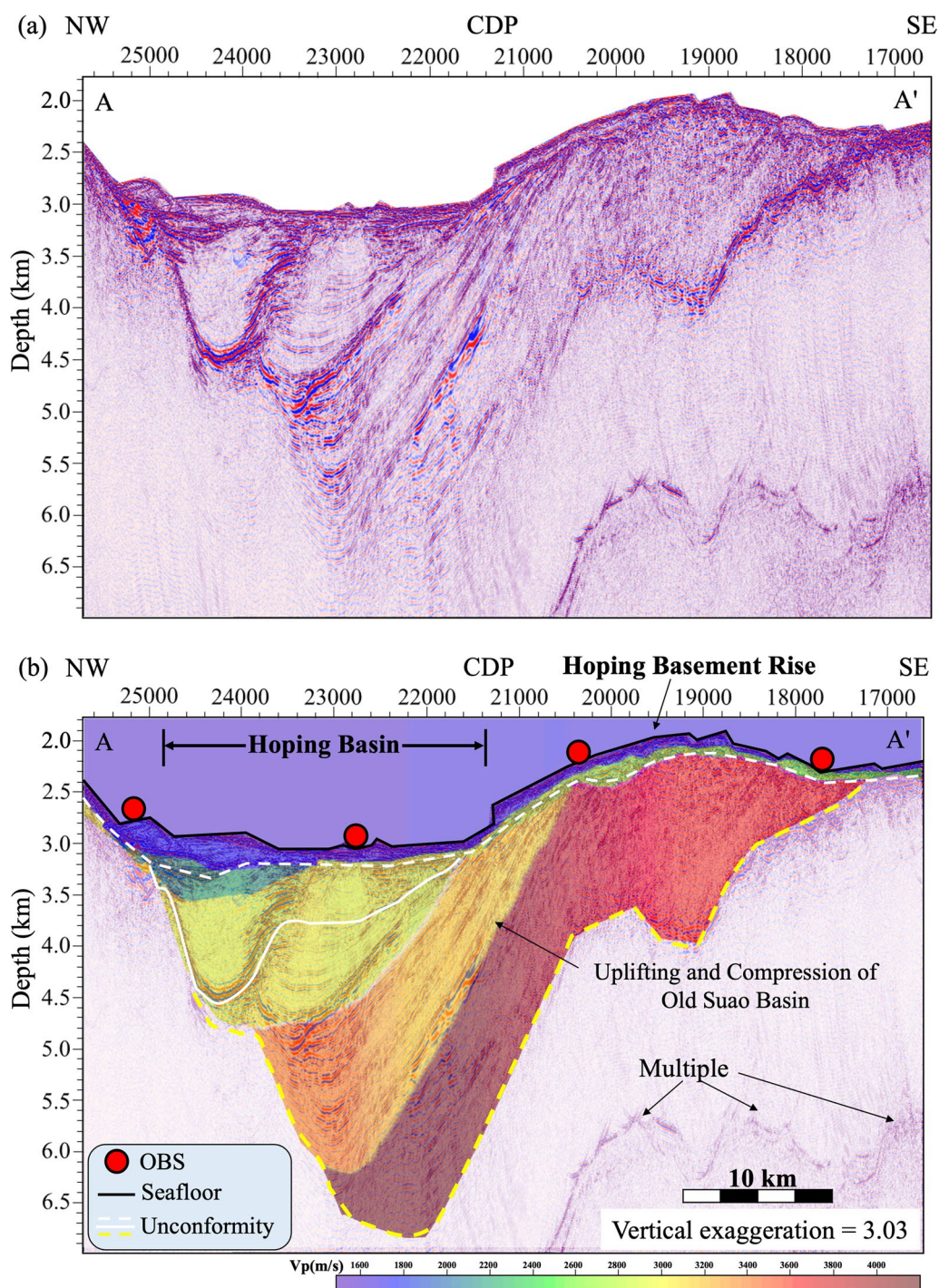


Fig. 3 **a** The uninterpreted PSDM section and **b** the horizontal velocity model is superimposed on the PSDM section with interpretations across the Hopping Basin along Line AA' (Fig. 2) of MGL0906-22

The quality of the hydrophone components of the OBS data was better; therefore, we used them to select the travel times (Figs. 7 and 8). These selected arrivals were superimposed on the vertical component of the OBS data to further check any additional signals.

Moreover, unnecessary signals were muted above the first arrivals to improve the display of the OBS data (Figs. 7 and 8). The curve of the first arrival varied significantly at an offset of approximately 52 km in OBS10 (red arrow in Fig. 8j). The variation in the

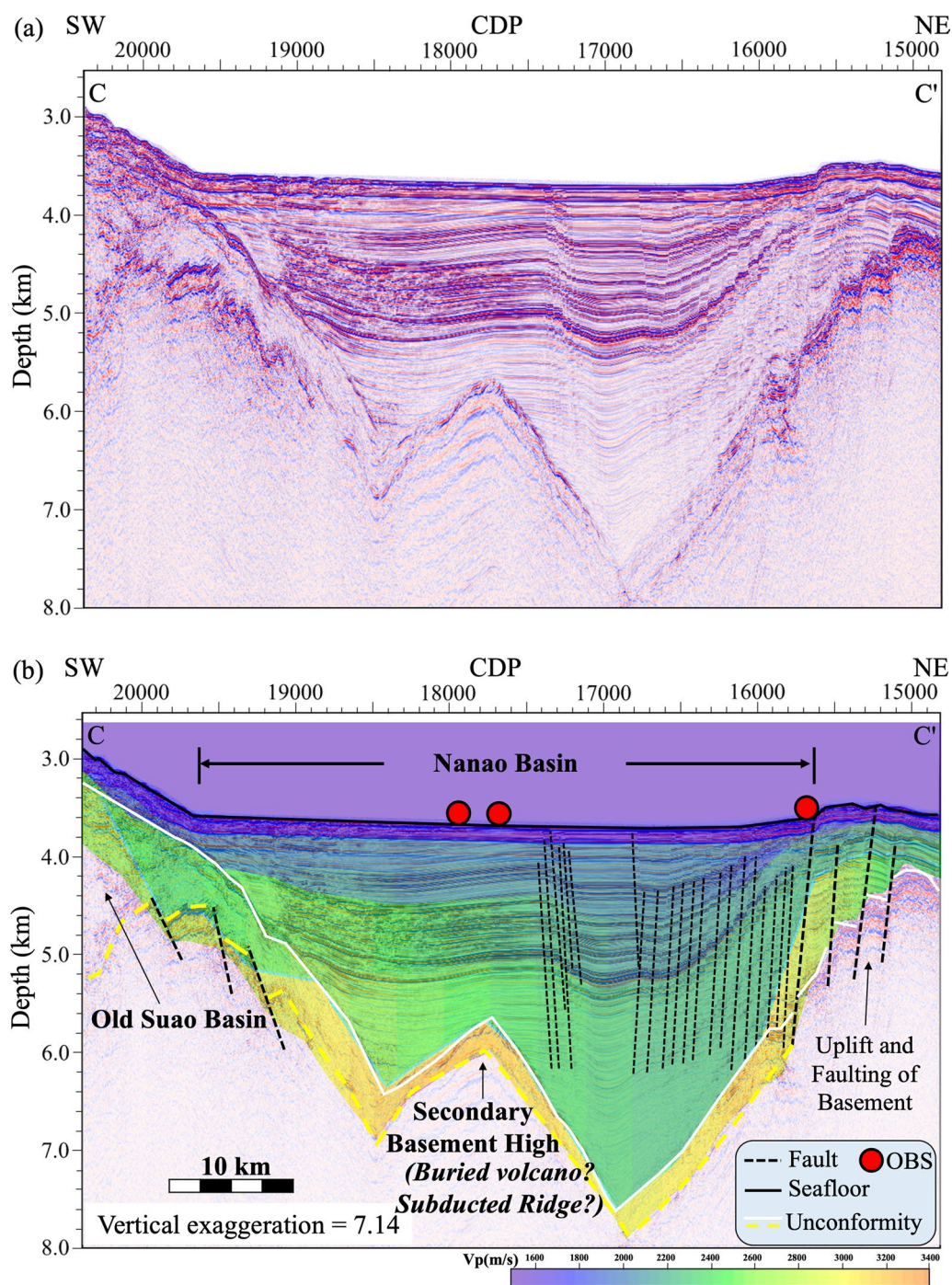


Fig. 4 Along Line CC' (Fig. 2) of EW9509-14, **a** the uninterpreted PSDM section and **b** the horizontal velocity model is superimposed on the PSDM section with interpretations across the Nanao Basin

first arrivals was found near the pop-up structures of the lower crust (e.g., Font and Lallemand 2009) existing along MGL0906-22. Travel-time errors indicate the model uncertainties of the P-wave velocity and the interface depth. Based on the ray density

along MGL0906-19 (Additional file 1: Fig. S9a) and MGL0906-22 (Additional file 1: Fig. S10a), the higher densities (number of rays/cell > 60) of the refracted and reflected rays traveled through complex structures causing higher travel-time errors (> 100 ms) in

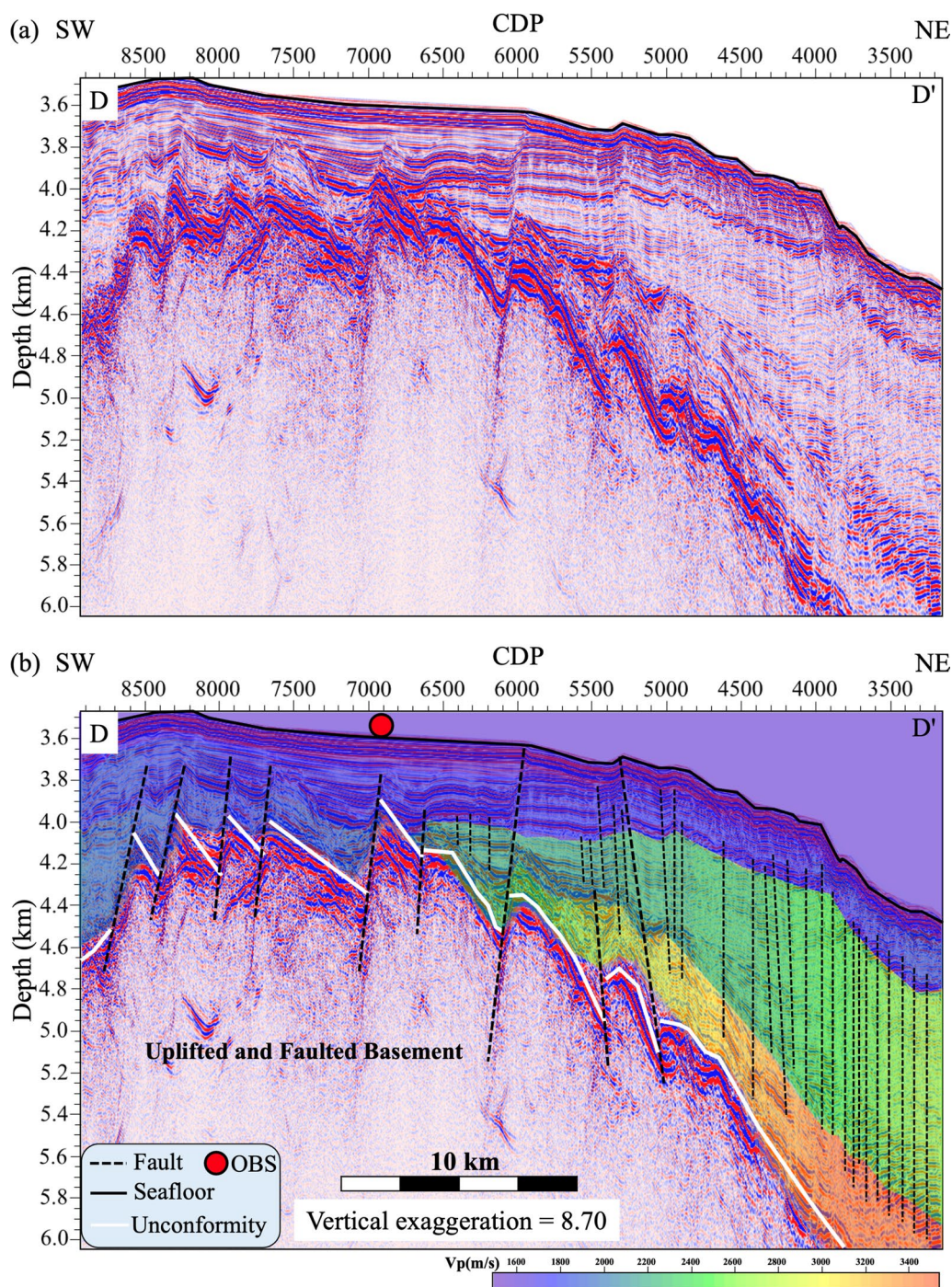


Fig. 5 **a** The uninterpreted PSDM section and **b** the horizontal velocity model is superimposed on the PSDM section with interpretations across the Nanao Basement Rise along Line DD' (Fig. 2) of MGL0906-22

the initial models. Most of the errors were reduced to 50–100 ms (the bold numbers in Tables 2 and 3) after many iterations of the model inversion process. Nevertheless, some of the errors for P-wave arrivals are still higher than 100 ms (the italic numbers in Tables 2

and 3) in the final model (Figs. 9 and 10). In summary, most of the velocities and interfaces in the final models (Figs. 9 and 10) with smaller errors (Tables 2 and 3) provide better insights than those of previous models (Additional file 1: Fig. S11). Based on the density

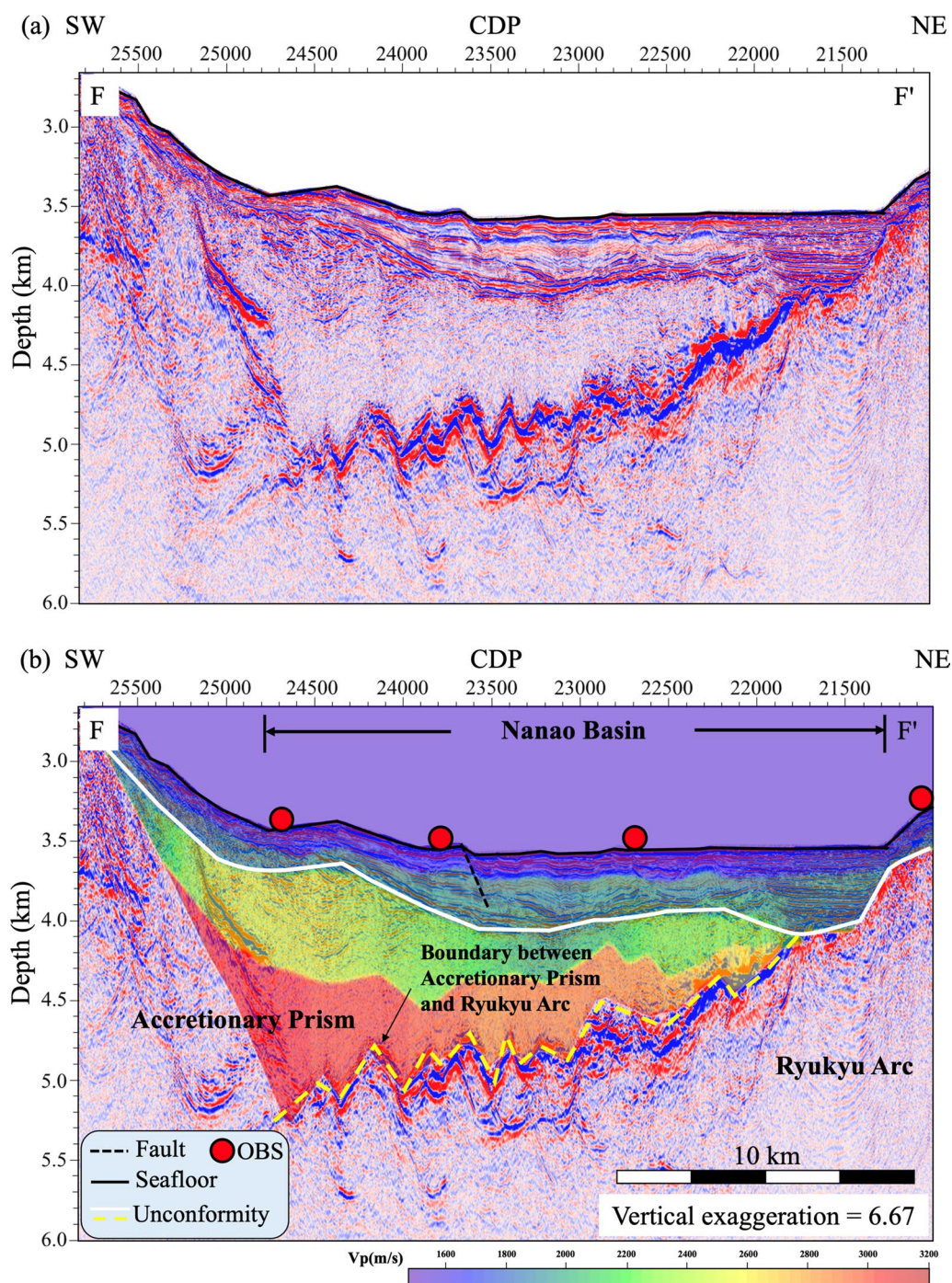


Fig. 6 **a** The uninterpreted PSDM section and **b** the horizontal velocity model is superimposed on the PSDM section with interpretations across the Nanao Basement Rise along Line FF' (Fig. 2) of MGL0906-12

of reflected and refracted rays in the cell dimension of 0.5 km × 0.5 km (Additional file 1: Figs. S9a and S10a), the rays (number of rays/cell > 30) cover most of the P-wave velocity-interface model. The ray coverage at

the end of the model and distances of 30–70 km and 80–100 km in the deep structures (Additional file 1: Fig. S10a) is lower; therefore, these parts of the model were masked to avoid over-interpreting the results.

3.3 Model uncertainty

In this study, totals of 9003 and 7702 rays were used to invert the velocity-interface models with total RMS travel-time errors of 58 ms and 75 ms along MGL0906-19

(Fig. 9) and MGL0906-22 (Fig. 10), respectively. To test model uncertainties, 843 (MGL0906-19) and 116 (MGL0906-22) preferred models within the quality threshold (ray number >70%; total RMS travel-time

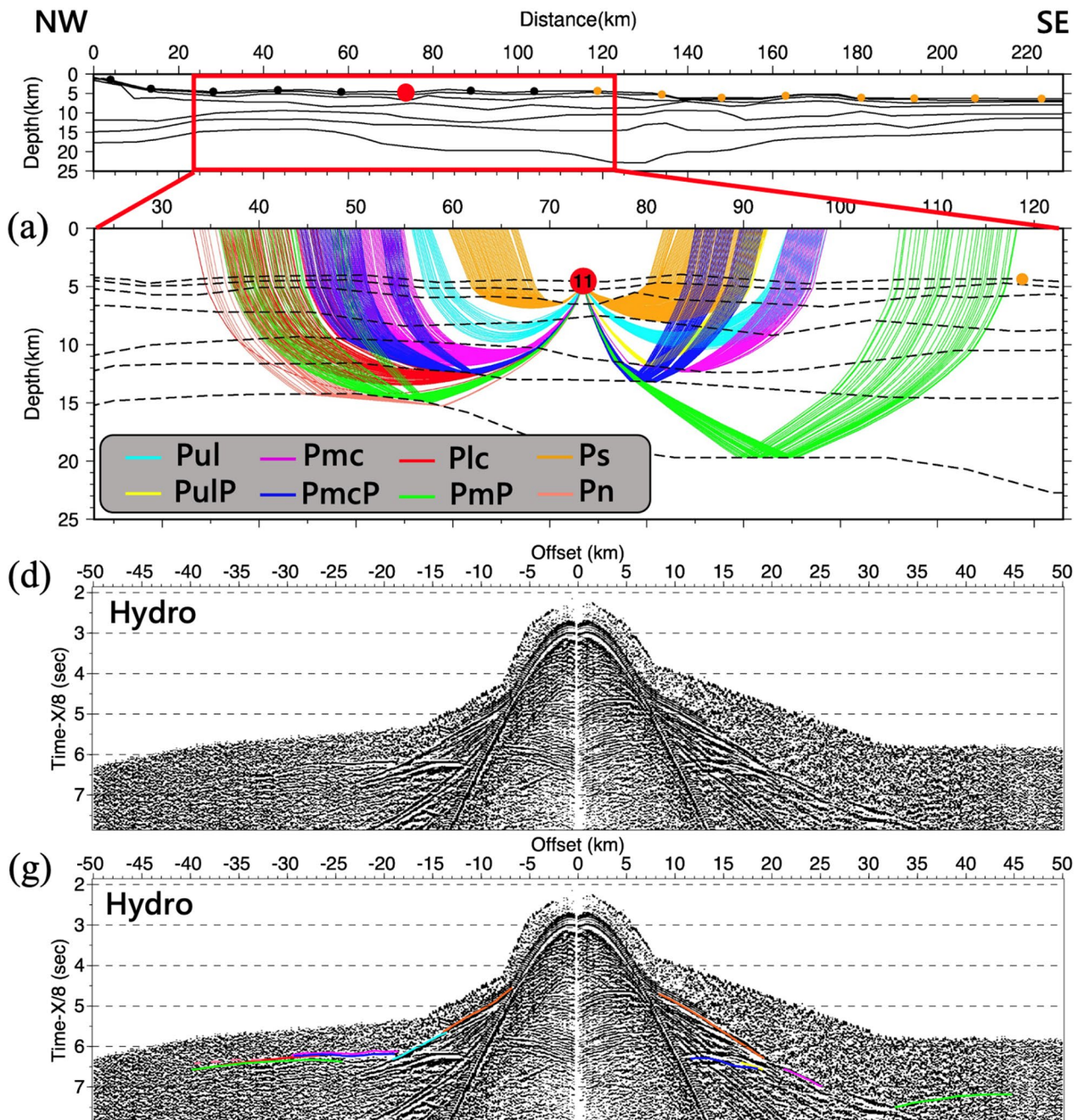


Fig. 7 The ray coverage of the picked arrivals from **a** OBS11, **b** OBS06, and **c** OBS03 station along MGL0906-19. The hydrophone component of **d** OBS11, **e** OBS06, and **f** OBS03 data without interpretation along MGL0906-19. The picked arrivals propagating through the crust superimposed on the **g** OBS11, **h** OBS06, and **i** OBS03 data along MGL0906-19. The OBS images of the blue and red frames respectively at the NW and SE offsets are zoomed in. Ps: arrivals refracted through the sediment; Pul: arrivals refracted through the upper layer (the upper crust or the accretionary prism); Pmc: arrivals refracted through the middle crust; Plc: arrivals refracted through the lower crust; PulP: arrivals reflected at the bottom of the upper layer (the upper crust or the bottom of the Ryukyu accretionary); PmcP: arrivals reflected at the intra-crustal interfaces; PmP: arrivals reflected at Moho. The dashed lines indicate less reliable picks

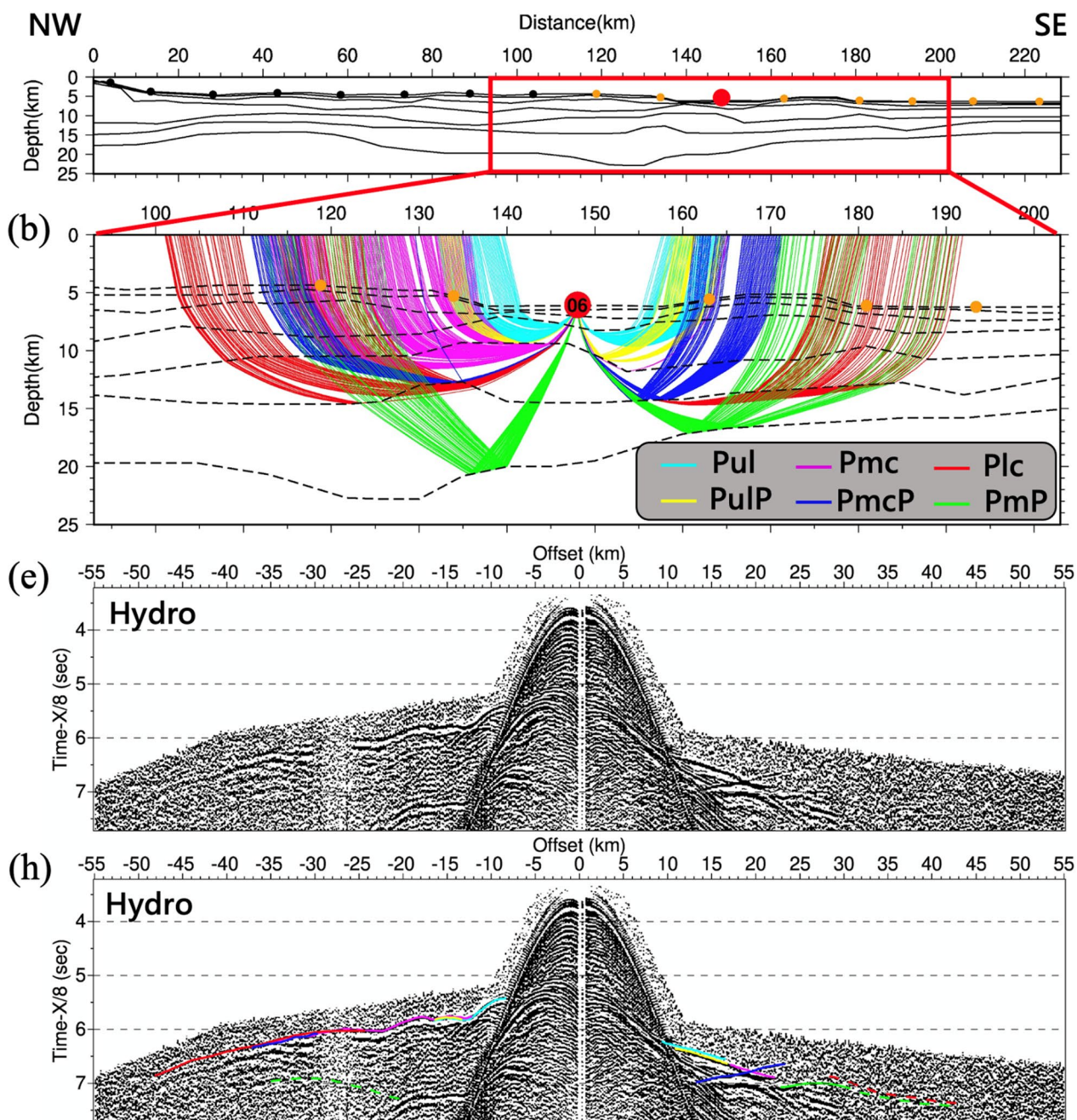


Fig. 7 continued

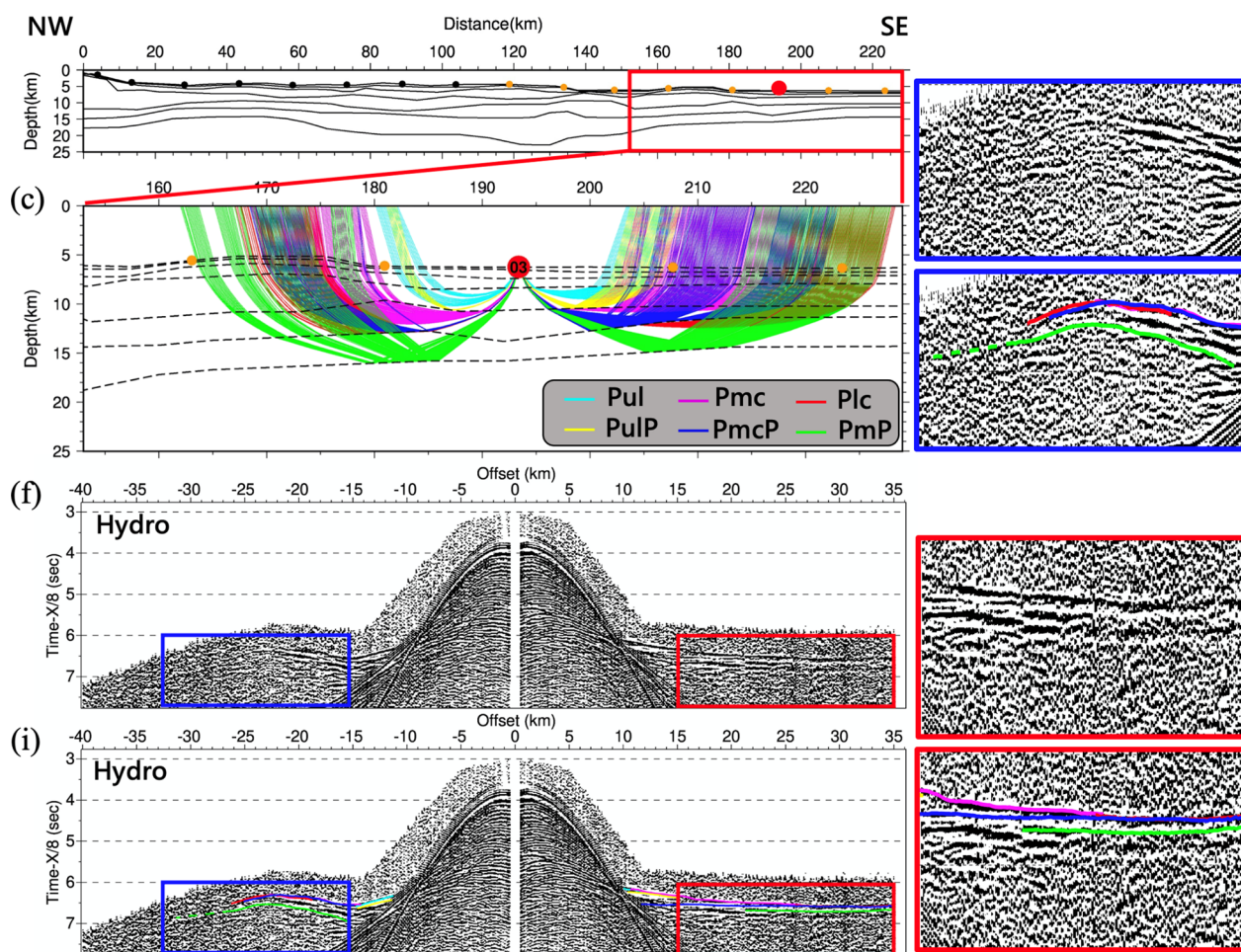


Fig. 7 continued

error < 110 ms) were selected from 40,000 models that had been created randomly using VMONTECARLO software (Loureiro et al. 2016). Based on these preferred models, the velocity uncertainty, and minimum and maximum interface depths were calculated, as shown in Additional file 1: Figs. S9b and S10b.

From the results of the model uncertainties along MGL0906-19 (Additional file 1: Fig. S9b) and MGL0906-22 (Additional file 1: Fig. S10b), most of the velocity uncertainties are ± 0.3 km/s and ± 0.5 km/s, respectively. Large values of velocity uncertainties near the interfaces along MGL0906-19 (Additional file 1: Fig. S9b) and MGL0906-22 (Additional file 1: Fig. S10b) were affected by interface uncertainties (green dotted and dashed lines in Additional file 1: Figs. S9b and S10b). The minimum (green dotted lines in Additional file 1: Figs. S9b and S10b) and maximum (green dashed lines in Additional file 1: Figs. S9b and S10b) interface depths were calculated from the preferred models to estimate the interface uncertainties along MGL0906-19 (± 0.3 km) and

MGL0906-22 (± 0.6 km). Based on the model uncertainty assessment, the preferred models within the quality threshold were similar to the velocity-interface models along MGL0906-19 (Fig. 9) and MGL0906-22 (Fig. 10). Therefore, the complex structures (e.g., pop-up structures and subducted Gagua Ridge) have been reliably derived in the models.

4 Results and discussion

In the present study, the ray coverages of the velocity-interface models were lower than those of the models of van Avendonk et al. [(2014, 2016); Additional file 1: Fig. S11] because these models were inverted by adding land stations to discuss the deep crustal structure of an arc-continent collision. To analyze the relationship between shallow structures and the subducted Gagua Ridge, the sedimentary structures of the velocity-interface models were well constrained by the PSDM sections of the LMCS data along MGL0906-19 and MGL0906-22 (Figs. 3, 5 and Additional file 1: Fig. S5). Subsequently,

the crustal structures of the velocity-interface models were built by performing a layer-by-layer inversion (Zelt and Smith 1992) from seismic tomography models (van Avendonk et al. 2014, 2016) to reduce errors of refracted and reflected arrivals which are smaller (Tables 2 and 3) than those in previous studies. Finally, six OBS profiles were integrated to observe variations in the sedimentary and crustal thickness, the geometry of the Ryukyu accretionary prism, and the structural uplift below the forearc basins. The sedimentary thickness was calculated from the seafloor to the basement, but the thickness of the Ryukyu accretionary prism was estimated from the seafloor to the bottom of the Ryukyu accretionary prism. The bottom of the Ryukyu accretionary prism was determined from interfaces with a P-wave velocity

of ~5.2 km/s and locations of sedimentary structures because the velocity-interface models along MGL0906-19 (Figs. 9) and MGL0906-22 (Figs. 10) include many sedimentary structures. However, the boundary of the Ryukyu accretionary prism at the end of the models is difficult to be identified so that the prism boundary just follows the P-wave velocity of 5.0 km/s. Furthermore, the bottom of the sediments was defined by considering the interfaces and the variation of the P-wave velocities (e.g., the blue line in Fig. 9 and the red line in Fig. 10). Moreover, the crustal thickness was calculated from the seafloor to the shallower Moho so that a subducting slab beneath the accretionary prism and an overriding plate in the forearc system were identified, respectively. However, six OBS profiles in the southernmost Ryukyu subduction

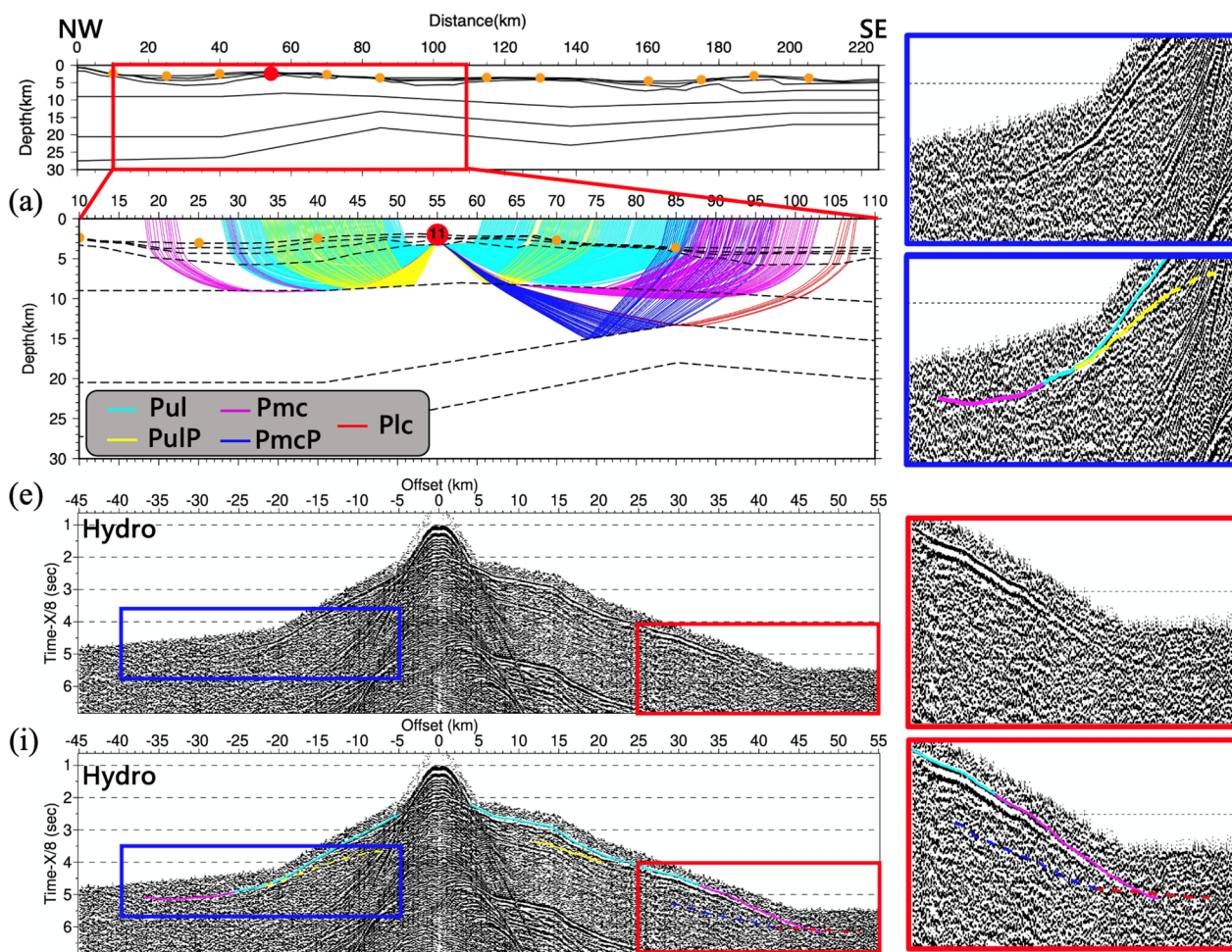


Fig. 8 The ray coverage of the picked arrivals from **a** OBS11, **b** OBS10, **c** OBS07, and **d** OBS02 station along MGL0906-22. The hydrophone component of **e** OBS11, **f** OBS10, **g** OBS07, and **h** OBS02 data without interpretation along MGL0906-22. The picked arrivals propagating through the crust superimposed on the **i** OBS11, **j** OBS10, **k** OBS07, and **l** OBS02 data along MGL0906-22. The OBS images of the blue and red frames respectively at the NW and SE offsets are zoomed in. The labels for arrivals are the same as those in Fig. 7. The dashed lines indicate less reliable picks. The red arrow in Fig. 8j indicates where the curve of the first arrival varies a lot

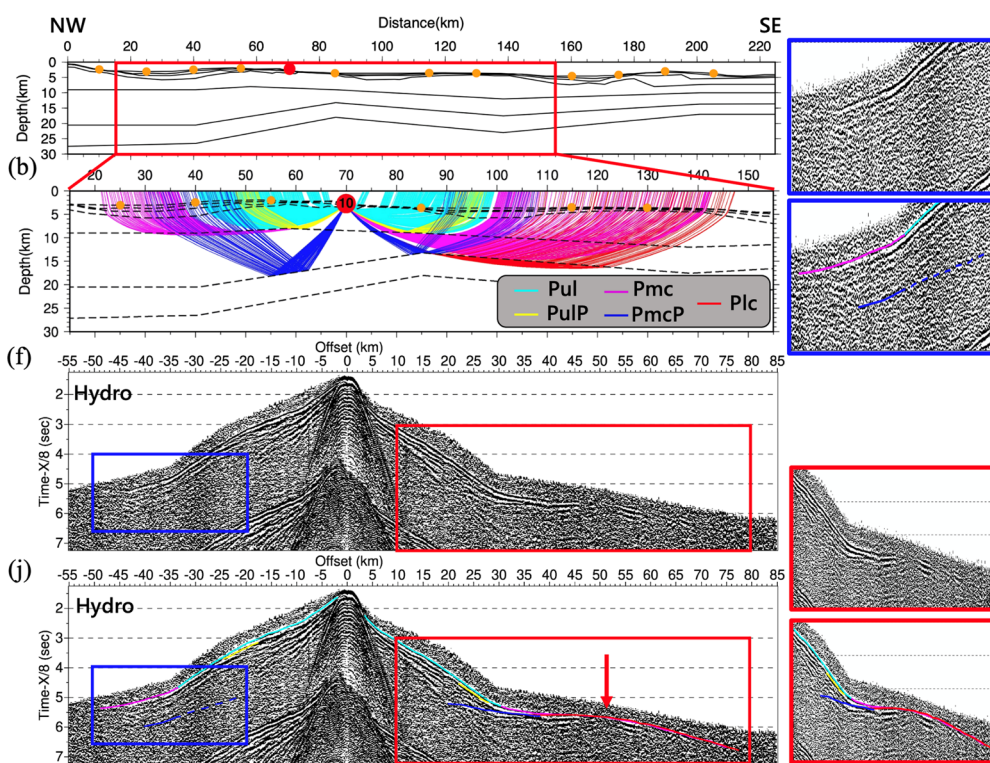


Fig. 8 continued

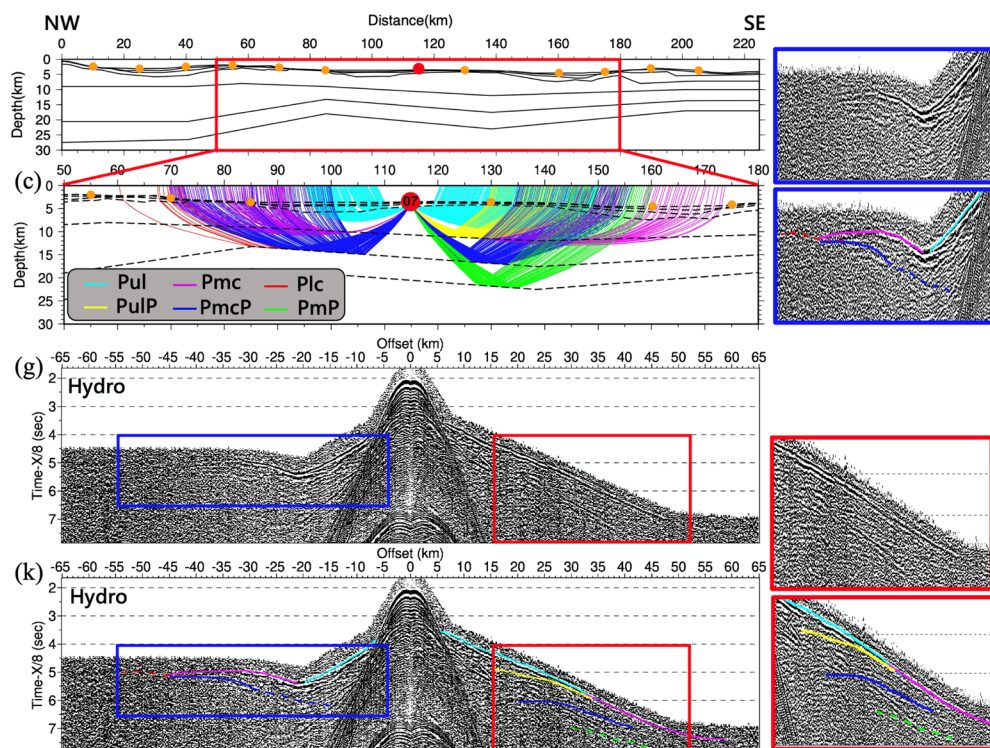


Fig. 8 continued

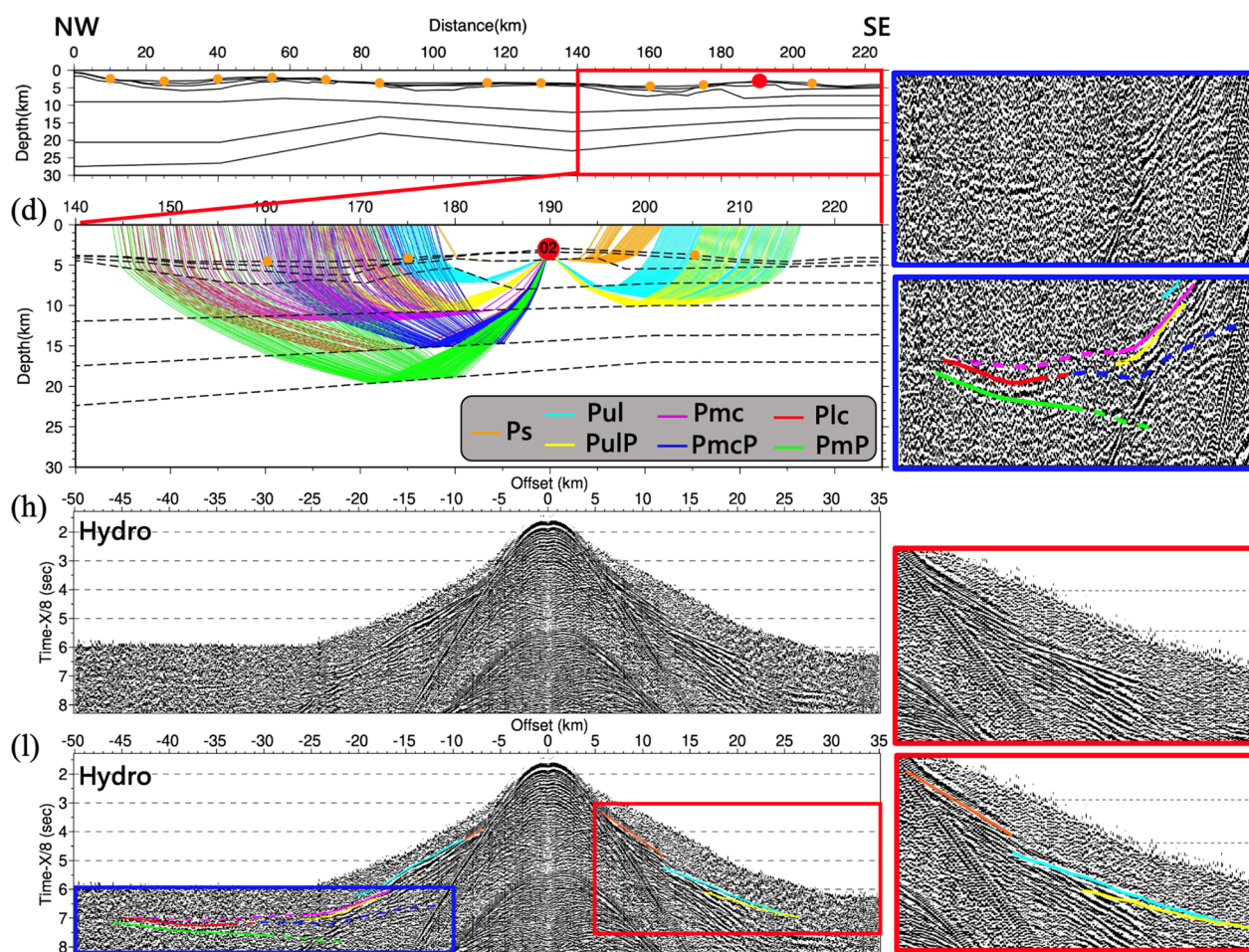


Fig. 8 continued

zone are too sparse to provide detailed maps of the sedimentary and crustal thickness. Nevertheless, interpolation between the six OBS profiles presented in this study reveals a general view of the variation of the sediment and the crust (Figs. 11 and 12).

4.1 Sedimentary structures across forearc basins

In the southernmost Ryukyu subduction zone, the Ryukyu basement is composed of morphologic highs and lows (Font et al. 2001). We observed two major basement highs, the Hoping (Fig. 3) and Nanao (Figs. 5 and Additional file 1: Fig. S6) Basement Rises, west and east of the Nanao Basin (Fig. 2), and a secondary basement high beneath the Nanao Basin (Fig. 4). Based on the PSDM section in the Nanao Basin along CC' (Fig. 4), the strata east of the secondary basement high were deformed by normal faults, and deeper than the strata west of the secondary basement high. Furthermore, many faults east of the secondary basement high in the Nanao Basin (Figs. 4b and Additional file 1: Fig. S5) have been formed

by the NW convergence of the PSP and subsequently converted to normal faults in the eastern portion of the Nanao Basin either by gravity or decoupling of the PSP and the Eurasian Plate (Hsu 2001). Thus, the secondary basement high beneath the Nanao Basin might be slightly uplifted by an asperity (e.g., the subducted Gagua Ridge or a buried volcano) to make the strata differently high from east to west. At the Nanao Basement Rise, the sedimentary thickness with a P-wave velocity of 1.6–3.4 km/s (Figs. 5b and Additional file 1: Fig. S6b) is ~1 km (Fig. 5b, Additional file 1: Figs. S6b, and 11). This basement high might have been formed by uplifting and been affected by numerous normal faults. These normal faults are cutting the uppermost sedimentary layer to reach the sea-floor because the Nanao Basement Rise is still active (Font et al. 2001). At the western Hoping Basement Rise, the west-dipping layers of the old Suao Basin with a sedimentary thickness of ~2 km and a P-wave velocity of 3.0–4.5 km/s were imaged (between common depth points of 17,200 and 23,800 in Fig. 3). The old Suao Basin

Table 2 RMS travel-time residual (ms) for P-wave arrivals at each station along MGL0906-19

OBS Station	16		15		14		13		12		11		10		09	
	W	E	W	E	W	E	W	E	W	E	W	E	W	E	W	E
Puc	-	<i>133</i>	84	75	38	40	47	72	27	93	95	<i>101</i>	75	42	84	-
PucP	-	8	38	10	86	-	-	39	31	54	-	11	55	-	86	77
Pmc	-	44	-	77	69	68	71	66	69	94	45	96	66	-	97	71
PmcP	-	69	-	22	96	23	91	79	35	51	49	26	32	-	-	41
Plc	-	-	-	-	96	39	45	93	12	26	10	-	61	10	-	23
PmP	-	-	-	-	21	41	66	22	12	14	48	12	82	16	22	33
Pn	-	-	-	-	-	15	87	40	-	-	5	-	38	21	-	-
OBS Station	08		07		06		05		04		03		02		01	
	W	E	W	E	W	E	W	E	W	E	W	E	W	E	W	E
Puc	44	43	72	44	87	55	68	56	45	49	60	45	84	83	40	-
PucP	94	-	40	63	90	82	52	42	52	60	35	35	32	27	39	62
Pmc	-	69	93	73	88	6	91	90	67	55	90	33	50	28	74	-
PmcP	63	55	51	92	42	76	39	20	17	61	47	52	44	49	71	-
Plc	14	32	13	10	21	28	5	38	73	66	56	69	-	82	30	-
PmP	25	79	25	29	13	28	26	12	67	84	56	50	-	20	17	-
Pn	-	-	-	-	-	-	-	-	-	-	-	-	-	-	-	-

Travel-time errors of 50–100 ms and greater than 100 ms are denoted by bold and italics emphasis, respectively

Table 3 RMS travel-time residual (ms) for P-wave arrivals at each station along MGL0906-22

OBS Station	14		13		12		11		10		09	
	W	E	W	E	W	E	W	E	W	E	W	E
Puc	-	47	86	69	85	98	70	95	94	<i>109</i>	<i>125</i>	70
PucP	-	13	70	57	-	-	18	15	48	25	-	60
Pmc	-	31	-	78	55	<i>128</i>	45	<i>114</i>	81	96	32	72
PmcP	-	70	-	-	-	19	-	70	45	34	27	30
Plc	-	-	-	-	-	-	-	63	-	<i>143</i>	-	99
PmP	-	-	-	-	64	84	-	-	-	-	-	34
OBS Station	07		06		04		03		02		01	
	W	E	W	E	W	E	W	E	W	E	W	E
Puc	91	72	98	<i>132</i>	95	49	54	31	67	72	<i>114</i>	27
PucP	-	32	73	26	40	25	11	20	15	36	-	-
Pmc	<i>126</i>	61	61	67	32	10	9	-	43	-	-	-
PmcP	29	20	15	22	20	-	35	-	40	-	-	24
Plc	34	-	51	52	76	-	98	-	7	-	-	-
PmP	-	48	38	42	66	-	33	33	76	-	73	46

Travel-time errors of 50–100 ms and greater than 100 ms are denoted by bold and italics emphasis, respectively

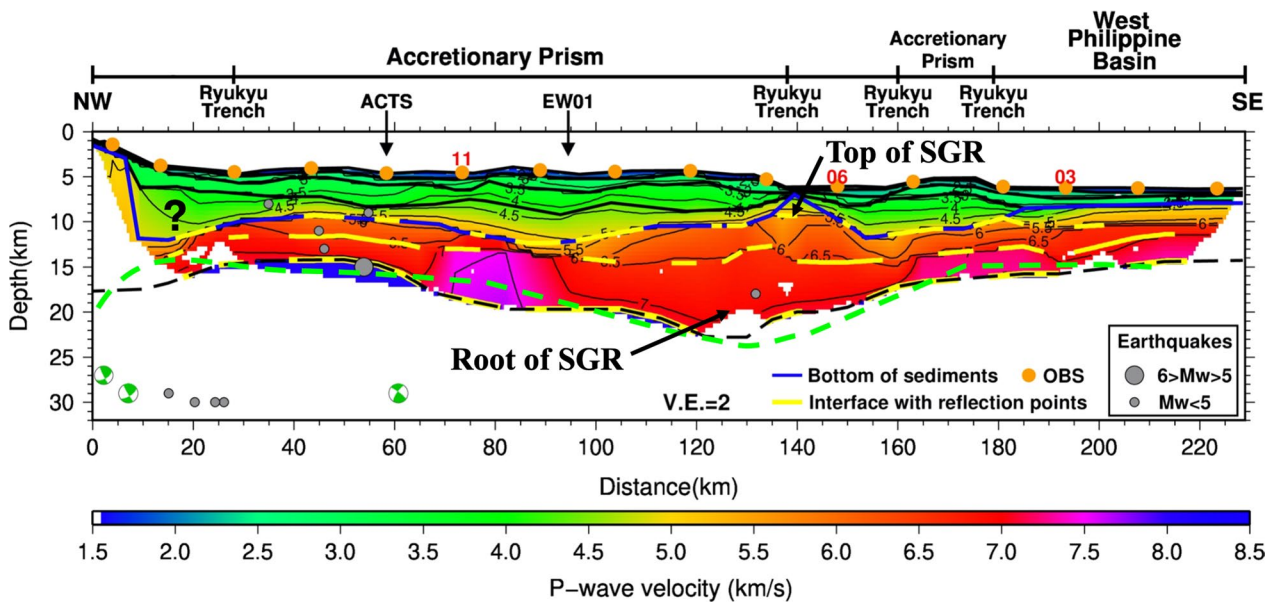


Fig. 9 The P-wave velocity-interface model covered by the refracted and reflected rays along MGL0906-19. The relocated earthquakes (Font et al. 2004) are superimposed on the model. The focal mechanisms of the earthquakes (BATS) are indicated by the green ($6 > M_w \geq 5$) beach balls. The black arrows show the location for the intersection of EW9509-01 (EW01) and MGL0906-12 (ACTS). The black dashed line shows the Moho. The Moho (defined by 7.5 km/s contour) from van Avendonk et al. (2014) is identified by the green line. SGR: Subducted Gagua Ridge

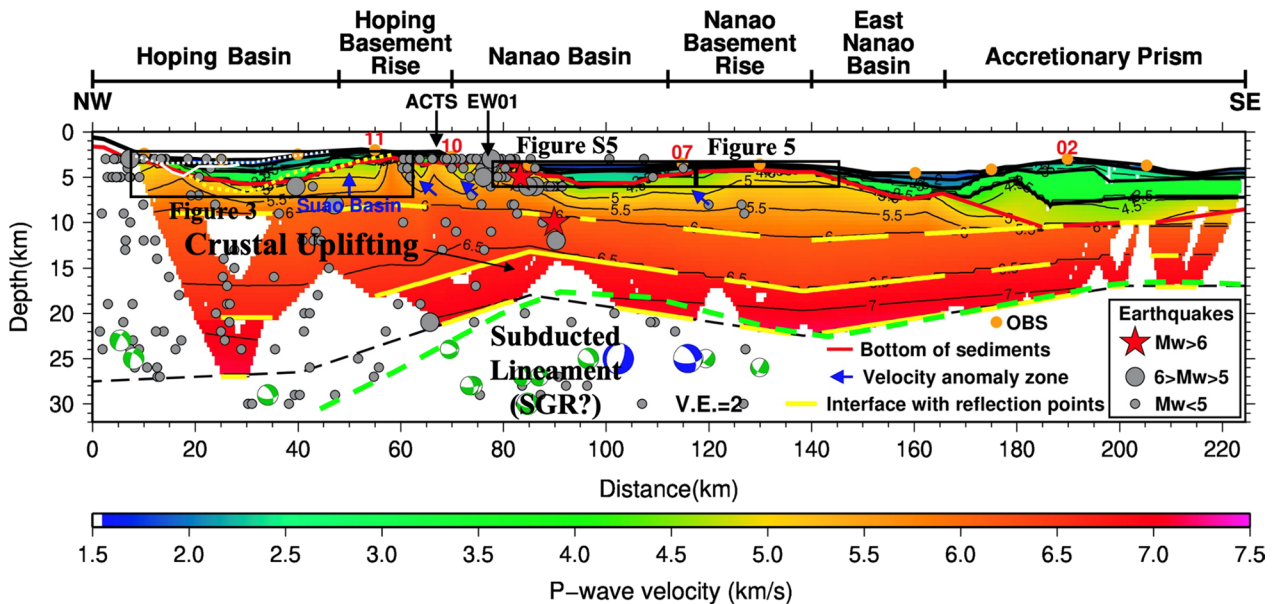


Fig. 10 The P-wave velocity-interface model covered by the refracted and reflected rays along MGL0906-22. The relocated earthquakes (Font et al. 2004) are superimposed on the model. The focal mechanisms of the earthquakes (BATS) are shown by the blue ($M_w \geq 6$) and green ($6 > M_w \geq 5$) beach balls, respectively. The black arrows show the location for the intersection of EW9509-01 (EW01) and MGL0906-12 (ACTS). The black frames show the areas of Figs. 3, 5 and Additional file 1: Fig. S5. The yellow dashed line, white line and white dashed line show the unconformities of the LMCS section in Fig. 3b. The Moho from van Avendonk et al. (2016) is identified by the green line. SGR: Subducted Gagua Ridge

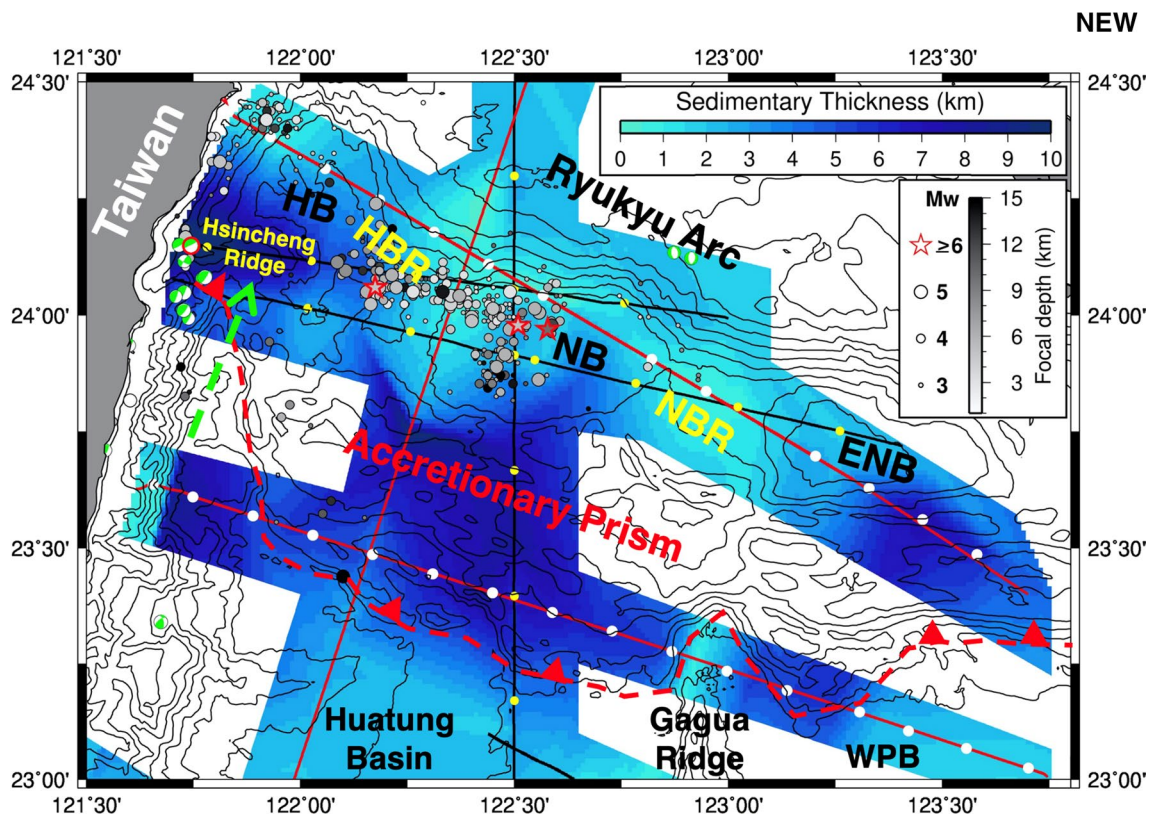


Fig. 11 The sedimentary thickness near the southernmost Ryukyu Trench superimposed by the relocated earthquakes at the depth of ≤ 15 km in 1992–1997 (Font et al. 2004). The red dashed line indicates the Ryukyu Trench with the red triangles which show the direction of subduction. The focal mechanisms of the earthquakes with the depth of ≤ 15 km are shown by the green ($6 > M_w \geq 5$) beach balls. The green dashed-line arrow shows the direction of the subducted PSP. The contour lines are bathymetry with the contour interval of 500 m. WPB: West Philippine Basin; HB: Hopping Basin; HBR: Hopping Basement Rise; NB: Nanao Basin; NBR: Nanao Basement Rise; ENB: East Nanao Basin

subsided first, followed by tectonic uplift after the deposition of sediments. The strata of the old Suao Basin have been observed to uplift with a westward dip, possibly due to the subduction of local asperities associated with the Hopping Basement Rise (Font et al. 2001). The P-wave velocity-interface model along MGL0906-22 (Fig. 10) confirms crustal uplifting beneath the Hopping Basement Rise, suggesting that the subducted Gagua Ridge may have caused this uplift as well as the secondary basement high beneath the Nanao Basin. Therefore, we propose that the subducted Gagua Ridge may have uplifted the old Suao Basin as well.

In the P-wave velocity-interface model along MGL0906-22 (Fig. 10), velocity anomaly zones (4.5–5.0 km/s), observed at the Hopping Basement Rise and the Nanao Basement Rise, may be formed by normal faults, such that these basement highs might be shallow active structures that can induce tsunamis in the southernmost Ryukyu subduction zone. Furthermore, these basement highs are separating the forearc basins at the southernmost Ryukyu subduction zone. In the Nanao Basin (the

P-wave velocity of 1.6–2.9 km/s), the maximum thickness is ~ 2.2 km in the northernmost part (Additional file 1: Fig. S5b) and ~ 4.2 km in the middle part (Fig. 4b). However, the sediments at the rear of the accretionary prism were covered beneath the Nanao Basin (Fig. 6) thus the sedimentary thickness is increased to ~ 5 km (Fig. 11). In the Hopping Basin, the PSDM section reveals the sedimentary thickness is 1.0–1.7 km with a P-wave velocity of 1.6–2.9 km/s (Fig. 3). However, the sedimentary image is without a clear layered structure (between the white dashed line and the white line in Fig. 3b), attesting to a lack of sedimentation, and is different from that of the other forearc basins. The sediments in the Hopping Basin may include turbidites and the old accretionary prism that was possibly formed by the Taiwan erosion and subduction of the PSP. Considering the west-dipping layers of the old Suao Basin (Fig. 3) and crustal uplift below the Hopping Basement Rise (Fig. 10), the Hopping Basin was formed because the old Suao Basin has subsided, uplifted, and was compressed.

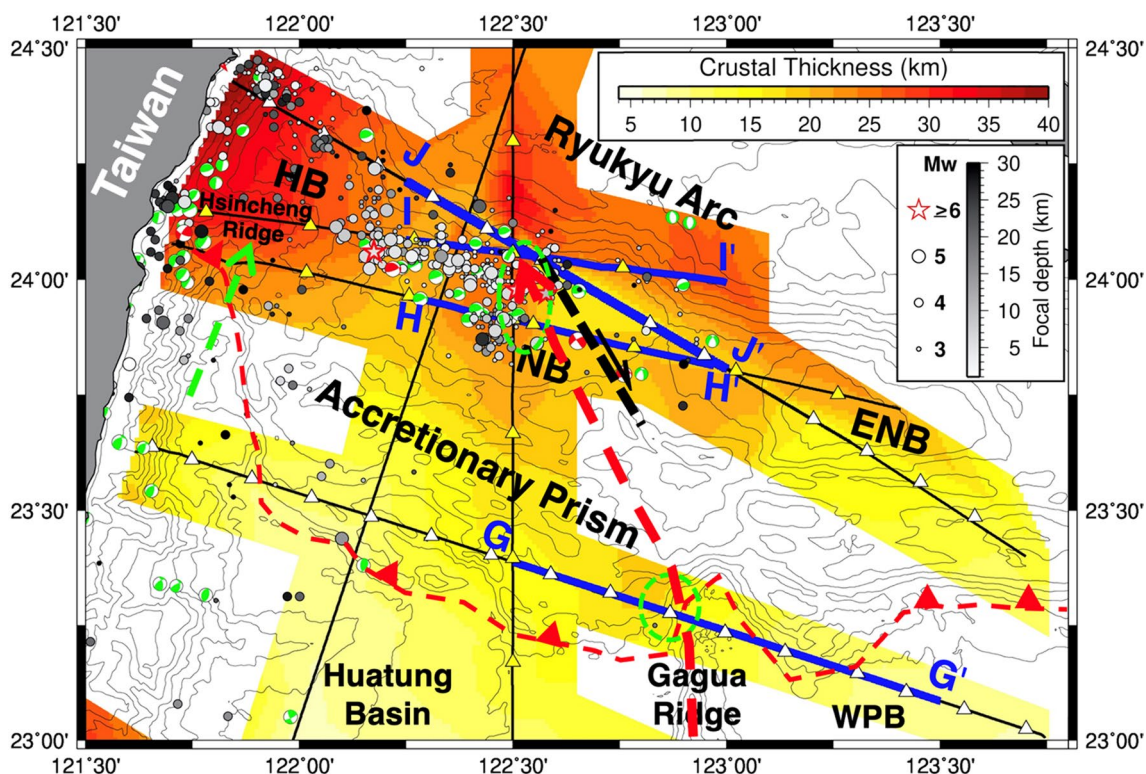


Fig. 12 The crustal thickness near the southernmost Ryukyu Trench superimposed by the relocated earthquakes in 1992–1997 (Font et al. 2004). The red dashed line indicates the Ryukyu Trench with the red triangles which show the direction of subduction. The focal mechanisms of the earthquakes with the depth of ≤ 30 km are shown by the red ($M_w \geq 6$) and green ($6 > M_w \geq 5$) beach balls. The location of uplifted structures is ranged by the green circles. The right-lateral strike-slip fault (Wang et al. 2019) is indicated by the black dashed line. The red and green dashed-line arrows show the directions of the obliquely subducted Gagua Ridge and the subducted PSP, respectively. The schematic diagram of the velocity-interfaces models along Lines GG', HH', II', and JJ' which, indicated by the blue lines, are shown in Fig. 13. The contour lines are bathymetry with the contour interval of 500 m. WPB: West Philippine Basin; HB: Hoping Basin; NB: Nanao Basin; ENB: East Nanao Basin

4.2 Accretionary prism in the southernmost Ryukyu subduction zone

The PSDM section along FF' (Fig. 6) images the Ryukyu subduction system, including the Ryukyu accretionary prism, the forearc basin, and the Ryukyu Arc, formed by the subduction of the PSP. Based on the velocity-interface models along MGL0906-19 (Fig. 9) and MGL0906-22 (Fig. 10), the thickness of the Ryukyu accretionary prism is 2.5–6.0 km with a P-wave velocity of 2.0–5.2 km/s. A similar P-wave velocity of the Ryukyu accretionary prism as 1.8–4.5 km/s in this study area was found (Wang et al. 2001, 2004; Klingelhoefer et al. 2012). Therefore, these velocity-interface models along EW9509-01 (Wang et al. 2001), EW9509-14 (Wang et al. 2004), EW9509-16 (Wang et al. 2004), MGL0906-12 (Klingelhoefer et al. 2012), MGL0906-19 (Fig. 9), and MGL0906-22 (Fig. 10) were integrated into isopach maps of sediment to delineate the geometry of the Ryukyu accretionary prism. Based on the isopach map of the sediments in the southernmost Ryukyu subduction zone, the Ryukyu accretionary prism is mostly parallel to the Ryukyu Trench (the

red dashed line with triangles in Fig. 11). The prism with a thickness of 4–10 km (Fig. 11) might extend northward to the NE coast of Taiwan Island.

Near the southernmost Ryukyu Trench, the bottom of the Ryukyu accretionary prism has been uplifted by the top of the subducted Gagua Ridge (Fig. 9), and the Ryukyu accretionary prism was recessed at the subducted Gagua Ridge (Fig. 11). The Ryukyu accretionary prism was deformed by the subducted Gagua Ridge, but the ridge has been subducted smoothly beneath the Ryukyu accretionary prism without causing shallow earthquakes (Figs. 9 and 11). However, in 2018 an earthquake ($M_w \sim 6.0$) with a depth of ~ 12 km below the Hsincheng Ridge near the NE coast of Taiwan Island (red circle in Fig. 11) was triggered by a thrust fault (the focal mechanism with the red circle in Fig. 11) near the décollement of the Ryukyu accretionary prism (~ 9 km deep) due to the PSP subducting northwardly at $\sim 121.8^\circ$ E (the green dashed-line arrow in Fig. 11). Thus, the results may show a high possibility that shallow earthquakes along the décollement of the Ryukyu accretionary prism

will be induced by the subduction of the PSP near the NE coast of Taiwan Island. Moreover, the unconformity with a depth of 4.0–5.3 km at the northernmost part of the Ryukyu accretionary prism below the Nanao Basin might be folded, fractured, or faulted (the yellow dashed line in Fig. 6b) by the NW convergence of the PSP to cause several shallow earthquakes (the grey circles in Fig. 11).

4.3 Structural uplift by obliquely subducted Gagua Ridge

South of the Ryukyu Trench, the thickness of the Gagua Ridge is ~15 km with a P-wave velocity of 5.0–7.0 km/s (Eakin et al. 2015; McIntosh et al. 2013). Near the southernmost Ryukyu Trench, the bottom of the Ryukyu accretionary prism was uplifted by the top of the subducted Gagua Ridge in the MCS sections (Tu 2015; van Avendonk et al. 2014). Similarly, the top and root of the subducted Gagua Ridge with a thickness of about 15 km and a P-wave velocity of 5.5–7.1 km/s were imaged near the southernmost Ryukyu Trench in the velocity-interface model along MGL0906-19 (Fig. 9). The irregular shape of the subducted Gagua Ridge may show that either the root of the subducted Gagua Ridge was shifted westward or the width of the subducted Gagua Ridge near the trench is larger than the width of the Gagua Ridge south of 23° N. Below the Nanao Basin, the Gagua Ridge might be subducted deeply northwestward to form the lower-crust uplift as shown in the velocity-interface model along MGL0906-22 (Fig. 10). However, the subducted Gagua Ridge may be located at a depth greater than 20 km which is too deep to image from this study. Furthermore, the basement uplifting and crustal uplifting due to the obliquely subducted Gagua Ridge can be revealed in a schematic diagram based on velocity-interface models along MGL0906-22 (Fig. 13a), EW9509-16 (Fig. 13b), EW9509-14 (Fig. 13c), and MGL0906-19 (Fig. 13d). Below the Nanao Basin and the Nanao Basement Rise, the basement uplifting (Figs. 4b and 13c), the thick crust (Fig. 13b and c), and the crustal uplifting (Fig. 13d) are observed. Moreover, the PSP below the Nanao Basin has been subducted beneath the Ryukyu Arc and the top of the subducted PSP was located at 15–25 km deep from south to north (Lallemand et al. 2013; Wang et al. 2001). Therefore, the sedimentary and crustal structures near ~122.5° E, ~24° N might be uplifted from south to north (the green circles in Fig. 12) by an asperity of the lineament (~25 km deep below the seafloor in Fig. 13).

This asperity had resulted in complex structures, including the subduction of an oceanic relief, seamount (Font and Lallemand 2009), and buckling of the subducted slab (Wang et al. 2004) observed beneath the Nanao Basin in previous studies. However, based on the width, location, and depth of the structural uplift, there is a low possibility of an off-scraped part of the Luzon Arc

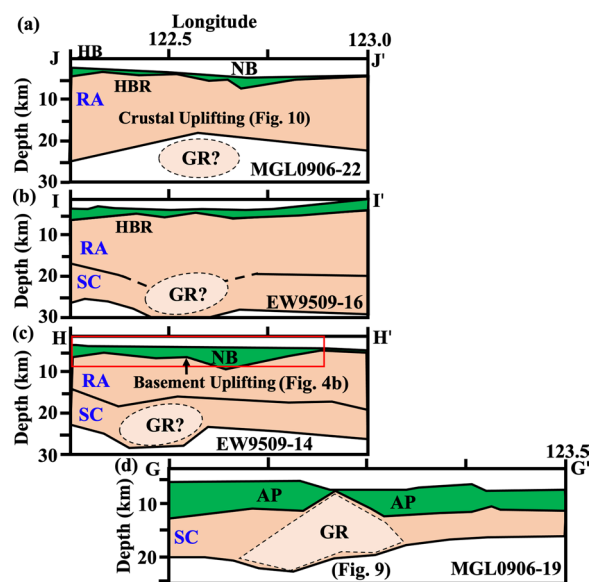


Fig. 13 The Schematic diagram of the obliquely subducted Gagua Ridge based on the velocity-interfaces models along **a** MGL0906-22, **b** EW9509-16 (Wang et al. 2004), **c** EW9509-14 (Wang et al. 2004), and **d** MGL0906-19. SC: Subducted Crust of PSP; RA: Ryukyu arc; GR: Gagua Ridge; AP: Accretionary Prism; NB: Nanao Basin; HB: Hoping Basin; HBR: Hoping Basement Rise

beneath the Nanao Basin (Font et al. 2001; Lallemand et al. 2013), because the width of the Luzon Arc (~50 km) is larger than the width of the Gagua Ridge (~25 km). Moreover, Schnurle et al. (1998) and Lallemand et al. (1999) suggested that the Gagua Ridge has been north-south-trending subducted to uplift the forearc basement which separates the Nanao and East Nanao Basins based on the MCS sections in the forearc basin system, but they did not image the crustal structures for identifying subduction of the Gagua Ridge. Considering the geometry of the ridge, the direction of plate convergence, and angles of subduction, the horizontal displacement of the subducted ridge at the accretive forearc (e.g., Gagua Ridge and Kyushu-Palau Ridge) was migrated toward the direction of plate convergence which was calculated by finite-element modeling (Zeumann and Hampel 2016). Dominguez et al. (1998) suggested that the Gagua Ridge is subducted toward the northwest (N344°) according to sandbox modeling and their MCS images. Based on the depth and location of the structural uplift (Fig. 13), and the previous studies (Dominguez et al. 1998; Zeumann and Hampel 2016), we preferred that this asperity is the subducted Gagua Ridge, and the ridge may have been obliquely subducted toward the northwest (red dashed-line arrow in Fig. 12) beneath the Ryukyu accretionary prism and below the Nanao Basin due to the NW convergence of the PSP.

Based on the velocity-interface model along MGL0906-22 (Fig. 10), many relocated earthquakes (Font et al. 2004) were near the seafloor and west of the lower-crust uplift between the Nanao Basin and the Hopping Basement Rise where they might have been induced by the lower-crust uplift and NW convergence of the PSP. Two major earthquakes with $M_w > 6$ (the red stars in Fig. 10) occurred at a shallow depth (< 12 km) above the uplift of the lower crust. The earthquakes were induced by thrust and strike-slip faults trending NW–SE at a depth of 20–30 km based on the focal mechanisms of the earthquakes near the crustal uplifting (blue and green beach balls in Fig. 10). These earthquakes in the vicinity of the Interplate Seismogenic Zone (ISZ) might have occurred because the PSP tearing is the locus of a seismic asperity responsible for an increase seismic coupling at the ISZ (Theunissen et al. 2012). Furthermore, the basement and crustal uplift were formed toward the northwest (red dashed-line arrows in Fig. 12) where shallow earthquakes (the circles in Fig. 12) are concentrated below the Nanao Basin and the Hopping Basement Rise, as shown in the isopach map of the crust. Thus, these shallow earthquakes below the Nanao Basin and the Hopping Basement Rise might be induced by the subduction of the Gagua Ridge.

South of the Ryukyu Trench, the Gagua Ridge with several fractured zones at the ridge top and both sides of the Gagua Ridge were observed (Deng et al. 2014; Deschamps et al. 1998). North of the Ryukyu Trench, the oceanic crust west of the subducted Gagua Ridge might be blocked to be difficultly subducted by the NW convergence of the PSP. Thus, the stress from the NW convergence of the PSP accumulated east of the obliquely subducted Gagua Ridge, generating many faults east of the secondary basement high beneath the Nanao Basin (Figs. 4b and Additional file 1: Fig. S5). This is one of the possibilities to form an NW–SE right-lateral strike-slip fault below the Nanao Basin (Wang et al. 2019, the black dashed line in Fig. 12) located NE of the fractured zones of Gagua Ridge which had been northwestwardly subducted. The NW convergence of the PSP might be blocked at the obliquely subducted Gagua Ridge to cause the transition from subduction to collision west of the obliquely subducted Gagua Ridge. Based on the results of finite-element modeling, the rate of vertical displacement of the obliquely subducted Gagua Ridge increased northwestwardly (Zeumann and Hampel 2016). In summary, we suggest that the uplift of the lower crust formed along the obliquely subducted Gagua Ridge, can induce shallow earthquakes below the forearc basins. Furthermore, the old Suao Basin might have been uplifted by the obliquely subducted Gagua Ridge to form the Hopping Basement Rise and the Hopping Basin.

5 Conclusion

The oblique subduction of the Gagua Ridge was deduced from sandbox (Dominguez et al. 1998) and finite-element (Zeumann and Hampel 2016) modeling. In this study, the bottom of the Ryukyu accretionary prism uplifted by the subducted Gagua Ridge was also observed from the velocity-interface model along MGL0906-19 near the southernmost Ryukyu Trench (Fig. 13d). In the forearc system north of the southernmost Ryukyu Trench, the basement (Fig. 13b and c) and crust (Fig. 13a) were uplifted from south to north by the asperity of the lineament (green circles in Fig. 12) which might be the subducted Gagua Ridge. Therefore, the Gagua Ridge may have been obliquely subducted toward the northwest (red dashed-line arrow in Fig. 12) beneath the Ryukyu accretionary prism and below the Nanao Basin to distribute the faults east of the secondary basement high by the NW convergence of the PSP (Fig. 4b). However, we cannot fully rule out the possibility that the Gagua Ridge has been north–south-trending subducted to uplift the forearc basement which separates the Nanao and East Nanao Basins because the isopach of sedimentary and the crustal thickness is poorly constrained at the Ryukyu accretionary prism. Moreover, uplifted structures might be formed by subduction of an oceanic relief, seamount (Font and Lallemand 2009), and buckling of the subducted slab (Wang et al. 2004). We need to collect more refraction data by using the active sources to image the crustal structures beneath the Ryukyu accretionary prism to justify the hypothesis of the obliquely subducted Gagua Ridge below the Nanao Basin.

Based on the hypothesis of the obliquely subducted Gagua Ridge, the shallow earthquakes of the thrust and strike-slip faults in a NW–SE trend (the circles and focal mechanisms in Fig. 12) were observed to be concentrated around the uplifted structures (the circles and focal mechanisms in Fig. 10) below the Nanao Basin and the Hopping Basement Rise. Many faults were formed in the eastern portion of the Nanao Basin (Figs. 4 and Additional file 1: Fig. S5) east of the obliquely subducted Gagua Ridge by the NW convergence of the PSP, and the faults were subsequently converted to normal faults by gravity or decoupling of the PSP and the Eurasian Plate (Hsu 2001). Furthermore, the Nanao Basement Rise is still uplifted and compressed to form a faulted basement and induce several faults that cut the uppermost sedimentary layer, reaching the seafloor (Figs. 5 and Additional file 1: Fig. S6). These faults in the Nanao Basement Rise and the eastern portion of the Nanao Basin may have moved readily to cause shallow earthquakes leading to tsunamis. West of the obliquely subducted Gagua Ridge, the old Suao Basin was uplifted and compressed to form the Hopping Basement Rise and the Hopping Basin

by collision. However, an earthquake ($M_w \sim 6.0$) in 2018 below the Hsincheng Ridge (red circle in Fig. 11) that occurred by a thrust fault (the focal mechanism in Figs. 1 and 11) near the décollement of the Ryukyu accretionary prism extended northwestwardly to the NE coast of Taiwan Island because the PSP is subducting northwardly at 121.8° E (green dashed-line arrow in Fig. 11). Thus, we suggest that shallow earthquakes near the southern end of the Ryukyu Trench at $\sim 121.8^\circ$ E may have been generated along the décollement of the Ryukyu accretionary prism near the NE coast of Taiwan Island. Furthermore, shallow earthquakes at depth of < 30 km may occur easily around the uplifted structure between the Hopping basement Rise and the Nanao Basin due to the obliquely subducted Gagua Ridge.

Supplementary Information

The online version contains supplementary material available at <https://doi.org/10.1007/s44195-023-00039-1>.

Additional file 1. Supplementary Figures.

Acknowledgements

This study was supported by the Ministry of Science and Technology (MOST) in Taiwan (MOST104-2611-M-019-021 and MOST108-2116-M-492-008-MY2). We acknowledge the team of TAICRUST and TAIGER projects for collecting OBS and LMCS data at sea. We appreciated that Dr. Yvonne Font and Dr. Serge Lallemand kindly provided the data for the relocated earthquakes. The constructive comments from two anonymous reviewers and the editor Frédéric Deschamps to improve the manuscript are also thanked. For analyzing the seismic data and drawing figures in this study, the software, including Emerson software (GEODEPTH, etc.), Seismic Unix, RAYINV (Zelt and Smith, 1992), and Generic Mapping Tools (Wessel et al., 2019), are appreciated.

Author contributions

JMD: Conceptualization, Methodology, Software, Investigation, Data Curation, Writing-Original Draft, Writing-Review & Editing, Visualization, Project administration, Funding acquisition. TKW: Conceptualization, Methodology, Validation, Investigation, Resources, Data Curation, Writing-Review & Editing, Supervision, Project administration, Funding acquisition. SW: Methodology, Data Curation, Writing-Review & Editing. WTH: Software, Formal analysis. YJD: Software, Formal analysis. All authors read and approved the final manuscript.

Declarations

Competing interests

The authors declare that they have no competing interests.

Received: 4 July 2022 Accepted: 11 April 2023

Published online: 20 April 2023

References

- Arai R, Kodaira S, Yamada T, Takahashi T, Miura S, Kaneda Y, Nishizawa A, Oikawa M (2017) Subduction of thick oceanic plateau and high-angle normal-fault earthquakes intersecting the slab. *Geophys Res Lett* 44:6109–6115. <https://doi.org/10.1002/2017GL073789>
- Bowin C, Lu RS, Lee CS, Schouten H (1978) Plate convergence and accretion in Taiwan Luzon region. *AAPG Bull* 62:1645–1672. <https://doi.org/10.1306/C1EA5260-16C9-11D7-8645000102C1865>
- Chin SJ, Lin JY, Chen YF, Wu WN, Liang CW (2016) Transition of the Taiwan-Ryukyu collision-subduction process as revealed by ocean-bottom seismometer observations. *J Asian Earth Sci* 128:149–157. <https://doi.org/10.1016/j.jseaes.2016.07.008>
- Chou HC, Kuo BY, Chiao LY, Zhao D, Hung SH (2009) Tomography of the westernmost Ryukyu subduction zone and the serpentinization of the fore-arc mantle. *J Geophys Res* 114:B12301. <https://doi.org/10.1029/2008JB006192>
- Cloos M (1992) Thrust-type subduction-zone earthquakes and seamount asperities: a physical model for seismic rupture. *Geology* 20:601–604. [https://doi.org/10.1130/0091-7613\(1992\)020%3c0601:TTSZEA%3e2.3.CO;2](https://doi.org/10.1130/0091-7613(1992)020%3c0601:TTSZEA%3e2.3.CO;2)
- Collot JY, Marcaillou B, Sage F, Michaud F, Agudelo W, Charvis P, Graindorge D, Gutscher MA, Spence G (2004) Are rupture zone limits of great subduction earthquakes controlled by upper plate structures? Evidence from multichannel seismic reflection data acquired across the northern Ecuador-southwest Colombia margin. *J Geophys Res* 109:B11103. <https://doi.org/10.1029/2004JB003060>
- Deng JM, Wang TK, Yang BJ, Lee CS, Liu CS, Chen SC (2012) Crustal velocity structure off SW Taiwan in the northernmost South China Sea imaged from TAIGER OBS and MCS data. *Marine Geophys Res* 33:327–349. <https://doi.org/10.1007/s11001-013-9166-8>
- Deng JM, Wang TK, Chen TR, Lee CS, Liu CS (2014) Crustal velocity structures imaged from four-component OBS data across the southern Gagua Ridge in the Western Philippine Sea. *Terr Atmos Ocean Sci* 25:755–773. [https://doi.org/10.3319/TAO.2014.08.28.01\(T\)](https://doi.org/10.3319/TAO.2014.08.28.01(T))
- Deschamps A, Lallemand S (2002) The West Philippine Basin: an eocene to early oligocene back arc basin opened between two opposed subduction zones. *J Geophys Res* 107:2322. <https://doi.org/10.1029/2001JB001706>
- Deschamps A, Lallemand S, Collot JY (1998) A detailed study of the Gagua Ridge: a fracture zone uplifted during a plate reorganisation in the Mid-Eocene. *Mar Geophys Res* 20:403–423. <https://doi.org/10.1023/A:1004650323183>
- Dominguez S, Lallemand S, Malavieille J, Schnürle P (1998) Oblique subduction of the Gagua Ridge beneath the Ryukyu accretionary wedge system: insights from marine observations and sandbox experiments. *Marine Geophys Res* 20:383–402. <https://doi.org/10.1023/A:1004614506345>
- Eakin DH, McIntosh K, van Avendonk HJA, Lavie L (2015) New geophysical constraints on a failed subduction initiation: the structure and potential evolution of the Gagua Ridge and Huatung Basin. *Geochem Geophys Geosyst* 16:380–400. <https://doi.org/10.1002/2014GC005548>
- Font Y, Lallemand S (2009) Subducting oceanic high causes compressional faulting in southernmost Ryukyu forearc as revealed by hypocentral determinations of earthquakes and reflection/refraction seismic data. *Tectonophysics* 466:255–267. <https://doi.org/10.1016/j.tecto.2007.11.018>
- Font Y, Liu CS, Schnürle P, Lallemand S (2001) Constraints on backstop geometry of the southwest Ryukyu subduction based on reflection seismic data. *Tectonophysics* 333:135–158. [https://doi.org/10.1016/S0040-1951\(00\)00272-9](https://doi.org/10.1016/S0040-1951(00)00272-9)
- Font Y, Kao H, Lallemand S, Liu CS, Chiao LY (2004) Hypocentre determination offshore of eastern Taiwan using the Maximum Intersection method. *Geophys J Int* 158:655–675. <https://doi.org/10.1111/j.1365-246X.2004.02317.x>
- Gautier S, Tiberi C, Lopez M, Foix O, Lallemand S, Theunissen T, Hwang C, Chang E (2019) Detailed lithospheric structure of an arc-continent collision beneath Taiwan revealed by joint inversion of seismological and gravity data. *Geophys J Int* 218:586–600. <https://doi.org/10.1093/gji/ggz159>
- Hsu SK (2001) Lithospheric structure, buoyancy and coupling across the southernmost Ryukyu subduction zone: an example of decreasing plate coupling. *Earth Planet Sci Lett* 186:471–478. [https://doi.org/10.1016/S0012-821X\(01\)00261-8](https://doi.org/10.1016/S0012-821X(01)00261-8)
- Hsu SK, Yeh YC, Sibuet JC, Doo WB, Tsai CH (2013) A mega-splay fault system and tsunami hazard in the southern Ryukyu subduction zone. *Earth Planet Sci Lett* 362:99–107. <https://doi.org/10.1016/j.epsl.2012.11.053>
- Hu WT (2017) Pre-Stack Depth Migration of Long-Offset Reflection Data for Imaging Strata and Structures in Fore-arc Basins off East Taiwan. National Taiwan Ocean University, 54 pp, Master Thesis, in Chinese.

- Huang HH, Wu YM, Song X, Chang CH, Lee SJ, Chang TM, Hsieh HH (2014) Joint Vp and Vs tomography of Taiwan: Implications for subduction-collision orogeny. *Earth Planet Sci Lett* 392:177–191. <https://doi.org/10.1016/j.epsl.2014.02.026>
- Institute of Earth Sciences, Academia Sinica, Taiwan (1996) Broadband Array in Taiwan for Seismology. Institute of Earth Sciences, Academia Sinica, Taiwan. Other/Seismic Network. <https://doi.org/10.7914/SN/TW>
- Kao H, Chen WP (1991) Earthquakes along the Ryukyu-Kyushu Arc: strain segmentation, lateral compression, and the thermomechanical state of the plate interface. *J Geophys Res* 96:21443–21485. <https://doi.org/10.1029/91JB02164>
- Klingelhoefer F, Berthet T, Lallemand S, Schnürle P, Lee CS, McIntosh K, Theunissen T (2012) P-wave velocity structure of the southern Ryukyu margin east of Taiwan: results from the ACTS wide-angle seismic experiment. *Tectonophysics* 578:50–62. <https://doi.org/10.1016/j.tecto.2011.10.010>
- Kodaira S, Takahashi N, Nakanishi A, Miura S, Kaneda Y (2000) Subducted seamount imaged in the rupture zone of the 1946 Nankaido earthquake. *Science* 289:104–106. <https://doi.org/10.1126/science.289.5476.104>
- Konstantinou KI, Lee SJ, Font Y, Kao H (2011) Rupture at the flank of the subducted Gagua ridge: the 18 December 2001 earthquake (Mw 6.8) offshore eastern Taiwan. *Phys Earth Planet Inter* 189:80–91. <https://doi.org/10.1016/j.pepi.2011.07.010>
- Kuo-Chen H, Wu FT, Roecker SW (2012) Three-dimensional P velocity structures of the lithosphere beneath Taiwan from the analysis of TAIGER and related seismic data sets. *J Geophys Res* 117:B06306. <https://doi.org/10.1029/2011JB009108>
- Lallemand S (2014) Strain modes within the forearc, arc and back-arc domains in the Izu (Japan) and Taiwan arc-continent collisional settings. *J Asian Earth Sci* 86:1–11. <https://doi.org/10.1016/j.jseaes.2013.07.043>
- Lallemand S, Tsien HH (1997) An introduction to active collision in Taiwan. *Tectonophysics* 274:1–4. [https://doi.org/10.1016/S0040-1951\(96\)00294-6](https://doi.org/10.1016/S0040-1951(96)00294-6)
- Lallemand S, Liu CS, Dominguez S, Schnürle P, Malavieille J, the ACT Scientific Crew (1999) Trench-parallel stretching and folding of forearc basins and lateral migration of the accretionary wedge in the southern Ryukyus: a case of strain partition caused by oblique convergence. *Tectonics* 18:231–247. <https://doi.org/10.1029/1998TC900011>
- Lallemand S, Theunissen T, Schnürle P, Lee CS, Liu CS, Font Y (2013) Indentation of the Philippine Sea plate by the Eurasian plate in Taiwan: details from recent marine seismological experiments. *Tectonophysics* 594:60–79. <https://doi.org/10.1016/j.tecto.2013.03.020>
- Loureiro A, Afilhado A, Matias L, Moulins M, Aslanian D (2016) Monte Carlo approach to assess the uncertainty of wide-angle layered models: application to the Santos Basin, Brazil. *Tectonophysics* 683:286–307. <https://doi.org/10.1016/j.tecto.2016.05.040>
- Lundberg N, Reed DL, Liu CS, Lieske J (1997) Forearc-basin closure and arc accretion in the submarine suture zone south of Taiwan. *Tectonophysics* 274:5–23. [https://doi.org/10.1016/S0040-1951\(96\)00295-8](https://doi.org/10.1016/S0040-1951(96)00295-8)
- McIntosh K, van Avendonk H, Lavier L, Lester WR, Eakin D, Wu F, Liu CS, Lee CS (2013) Inversion of a hyper-extended rifted margin in the southern Central Range of Taiwan. *Geology* 41:871–874. <https://doi.org/10.1130/G34402.1>
- Mochizuki K, Yamada T, Shinohara M, Yamanaka Y, Kanazaw T (2008) Weak interplate coupling by seamounts and repeating M ~ 7 earthquakes. *Science* 321:1194–1197. <https://doi.org/10.1126/science.1160250>
- Moore GF, Bangs NL, Taira A, Kuramoto S, Pangborn E, Tobin HJ (2007) Three-dimensional splay fault geometry and implications for tsunami generation. *Science* 318:1128–1131. <https://doi.org/10.1126/science.1147195>
- Park JO, Tsuru T, Kodaira S, Cummins PR, Kaneda Y (2002) Splay fault branching along the Nankai subduction zone. *Science* 297:1157–1160. <https://doi.org/10.1126/science.1074111>
- Park JO, Hori T, Kaneda Y (2009) Seismotectonic implications of the Kyushu-Palau ridge subducting beneath the westernmost Nankai forearc. *Earth Planets Space* 61:1013–1018. <https://doi.org/10.1186/BF03352951>
- Plafker G (1972) Alaskan earthquake of 1964 and Chilean earthquake of 1960: implications for arc tectonics. *J Geophys Res* 77:901–925. <https://doi.org/10.1029/JB077i005p00901>
- Schnürle P, Liu CS, Lallemand S, Reed DL (1998) Structural insight into the south Ryukyu margin: effects of the subducting Gagua Ridge. *Tectonophysics* 288:237–250. [https://doi.org/10.1016/S0040-1951\(97\)00298-9](https://doi.org/10.1016/S0040-1951(97)00298-9)
- Sibuert JC, Rangin C, Le Pichon X, Singh S, Cattaneo A, Graindorge D, Klingelhoefer F, Lin JY, Malod J, Maury T, Schneider JL, Sultan N, Umber M, Yamaguchi H, the “Sumatra aftershocks” team (2007) 26th December great Sumatra-Andaman earthquake: coseismic and post-seismic motions in northern Sumatra. *Earth Planet Sci Lett* 263:88–103. <https://doi.org/10.1016/j.epsl.2007.09.005>
- Subrahmanyam C, Gireesh R, Chand S, Kamesh Raju KA, Gopala Rao D (2008) Geophysical characteristics of the Ninetyeast Ridge-Andaman island arc-trench convergent zone. *Earth Planet Sci Lett* 266:29–45. <https://doi.org/10.1016/j.epsl.2007.10.016>
- Taylor B, Goodliffe AM (2004) The West Philippine Basin and the initiation of subduction, revisited. *Geophys Res Lett* 31:L12602. <https://doi.org/10.1029/2004GL020136>
- Theunissen T, Lallemand S, Font Y, Gautier S, Lee CS, Liang WT, Wu F, Berthet T (2012) Crustal deformation at the southernmost part of the Ryukyu subduction (East Taiwan) as revealed by new marine seismic experiments. *Tectonophysics* 578:10–30. <https://doi.org/10.1016/j.tecto.2012.04.011>
- Tu NN (2015) Pre-Stack Depth Migration of Long-Offset Reflection Data for Imaging Velocity of Sedimentary and Crustal Structures in the Ryukyu Subduction Zone off East Taiwan. National Taiwan Ocean University, 72 pp, Master Thesis.
- van Avendonk HJA, Kuo-Chen H, McIntosh KD, Lavier LL, Okaya DA, Wu FT, Wang CY, Lee CS, Liu CS (2014) Deep crustal structure of an arc-continent collision: constraints from seismic traveltimes in central Taiwan and the Philippine Sea. *J Geophys Res* 119:8397–8416. <https://doi.org/10.1002/2014JB011327>
- van Avendonk HJA, McIntosh KD, Kuo-Chen H, Lavier LL, Okaya DA, Wu FT, Wang CY, Lee CS, Liu CS (2016) A lithospheric profile across northern Taiwan: from arc-continent collision to extension. *Geophys J Int* 204:331–346. <https://doi.org/10.1093/gji/ggv468>
- von Huene R, Ranero CR (2003) Subduction erosion and basal friction along the sediment-starved convergent margin off Antofagasta, Chile. *J Geophys Res* 108:2079. <https://doi.org/10.1029/2001JB001569>
- Wang TK, McIntosh K, Nakamura Y, Liu CS, Chen HW (2001) Velocity-interface structure of the southwestern Ryukyu subduction zone from EW9509-1 OBS/MCS data. *Marine Geophys Res* 22:265–287. <https://doi.org/10.1023/a:1014671413264>
- Wang TK, Lin SF, Liu CS, Wang CS (2004) Crustal structure of the southernmost Ryukyu subduction zone: OBS, MCS and gravity modeling. *Geophys J Int* 157:147–163. <https://doi.org/10.1111/j.1365-246X.2004.02147.x>
- Wang SY, Hsu SK, Yeh YC (2019) Earthquake-related structures beneath the southernmost portion of the Ryukyu Arc and Forearc. *Geophys Res Lett* 46:3717–3725. <https://doi.org/10.1029/2019GL082121>
- Wessel P, Luis JF, Uieda L, Scharroo R, Wobbe F, Smith WHF, Tian D (2019) The generic mapping tools version 6. *Geochem Geophys Geosyst* 20:5556–5564. <https://doi.org/10.1029/2019GC008515>
- Wu YM, Shyu JH, Chang CH, Zhao L, Nakamura M, Hsu SK (2009) Improved seismic tomography offshore northeastern Taiwan: implications for subduction and collision processes between Taiwan and the southernmost Ryukyu. *Geophys J Int* 178:1042–1054. <https://doi.org/10.1111/j.1365-246X.2009.04180.x>
- Yilmaz O (2001) Seismic data analysis: processing, inversion, and interpretation of seismic data, Series: Investigations in Geophysics, no. 10. Doherty, S. F., ed., SEG, Tulsa.
- Zelt CA, Smith RB (1992) Seismic travel time inversion for 2-D crustal velocity structure. *Geophys J Int* 108:16–34. <https://doi.org/10.1111/j.1365-246X.1992.tb00836.x>
- Zeumann S, Hampel A (2015) Deformation of erosive and accretive forearcs during subduction of migrating and non-migrating aseismic ridges: results from 3-D finite element models and application to the Central American, Peruvian, and Ryukyu margins. *Tectonics* 34:1769–1791. <https://doi.org/10.1002/2015TC003867>
- Zeumann S, Hampel A (2016) Three-dimensional finite-element models on the deformation of forearcs caused by aseismic ridge subduction: the role of ridge shape, friction coefficient of the plate interface and mechanical properties of the forearc. *Tectonophysics* 684:76–91. <https://doi.org/10.1016/j.tecto.2015.12.022>

Publisher's Note

Springer Nature remains neutral with regard to jurisdictional claims in published maps and institutional affiliations.